Observations *and* Classification of Echoes *with the* Polarimetric WSR-88D Radar

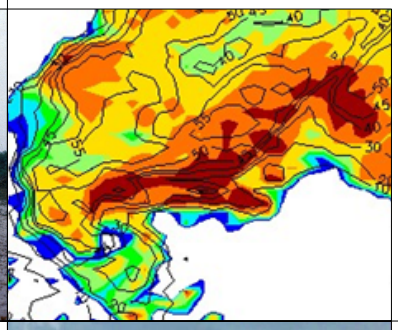

Prepared by:
T. Schuur, A. Ryzhkov,
and P. Heinselman

with contributions by:
D. Zrnić, D. Burgess,
and K. Scharfenberg

October 2003

National Oceanic and Atmospheric Administration
National Severe Storms Laboratory
Norman, Oklahoma

University of Oklahoma
Cooperative Institute for
Mesoscale Meteorological Studies

CONTENTS

PREAMBLE

Over the years NSSL has been providing technical information to the National Weather Service. This exchange had many forms, from formal reports and algorithms to consultation and supply of radar data in real time to the Weather Services Forecast Office. After the decision to evolve its network of WSR-88Ds to keep pace with emerging knowledge and technology the NWS provided a spare WSR-88D to NSSL. Hence, NSSL became the principal NOAA Laboratory for evolutionary and revolutionary enhancements of weather radar science and technology. At that time (mid nineties) Doppler Radar and Remote Sensing Research group committed to document in report form all significant innovations, changes, and results deemed of special value for operational applications regardless whether such writing was formally required. This is the fourteenth report in the series since 1997. It describes classification of polarimetric radar echoes. Applications are on data collected during the Joint POLarization Experiment (JPOLE) which was conducted from spring of 2002 until summer of 2003. I was fortunate to share the work on polarimetric upgrade of the research and development WSR-88D with scientists and engineers second to none. Allen Zahrai led the team of engineers who designed the new processor which enabled scanning strategies and allowed more flexibility than the old system. Mike Schmidt ably assisted with Richard Wahkinney made extensive modifications of microwave circuitry and controls. John Carter contributed to design of microwave circuits and with Valery Melnikov made numerous calibration measurements of the two channels. As always I relied on my colleague Dick Doviak for support, advice, and technical help. Alan Sigia, from Sigmet, resolved numerous technical details needed to operate the RVP7 processor in dual polarization mode. The Radar Operations Center (ROC) of NWS contributed the basic RVP7 processor and display, which was subsequently enhanced to process dual polarization signals.

This is the first year that NWS's Office of Science and Technology specifically and generously contributed to the dual polarization effort at NSSL. Thus the report represents our continuous commitment to NWS and is part of a cumulative contribution to the Office of Science and Technology.

October 2003 in Norman
Dusan S. Zrnic

1. Introduction

In the Spring of 2002, several years of effort on the NOAA research WSR-88D radar culminated in generation and display of dual polarization radar data and products. As part of the Joint Polarization Experiment (JPOLE), high quality polarimetric data sets were collected over the course of the next year. In total, data were collected for 98 meteorological and non-meteorological events. These data are catalogued both chronologically and by event-type, and subsequently described within an online database at http://cimms.ou.edu/~heinsel/jpole/database.html and http://cimms.ou.edu/~heinsel/jpole/stormtype.html, respectively. In this report, we present analyses that use this large dataset to demonstrate the polarimetric WSR-88D's ability to: (1) improve data quality, and (2) improve hydrometeor identification capabilities. Complementary reports present an analysis of the calibration and performance of the polarimetric NSSL WSR-88D (Melnikov et al. 2003), an overview of the JPOLE data collection and operational delivery (Schuur et al. 2003a), and an analysis of the ability of a polarimetric WSR-88D to improve rainfall estimation (Ryzhkov et al. 2003).

2. Description of the classification algorithm

One of the important advantages of polarimetric weather radar is its ability to discriminate between hydrometeor types and non-hydrometeor scatterers. Our classification algorithm is based on the principles of fuzzy logic as outlined in Vivekanandan et al. (1999), Zrnic and Ryzhkov (1999), Straka et al. (2000), Liu and Chandrasekar (2000), and Zrnic et al. (2001). According to fuzzy logic methodology, different hydrometeor classes are described by the one-dimensional or two-dimensional membership functions that are expressed as follows:

$$F^{(i)}(V_j) = P^{(i)}(V_j) \tag{1}$$

or

$$F^{(i)}(Z,V_j) = P^{(i)}(Z)\, P_Z^{(i)}(V_j) \tag{2}$$

In (1) and (2), Z is the radar reflectivity factor at horizontal polarization and V_j is the j^{th} additional radar variable (polarimetric or non-polarimetric). One-dimensional unconditional membership functions $P^{(i)}(Z)$ and $P_Z^{(i)}(V_j)$ characterize distributions[1] of Z and V_j for the i^{th} class, whereas the membership functions $P_Z^{(i)}(V_j)$ characterize conditional distribution of the variable V_j for the i^{th} class for a given Z. The product of $P^{(i)}(Z)$ and $P_Z^{(i)}(V_j)$ represents the two-dimensional membership function characterizing the joint distribution of Z and V_j in the $Z - V_j$ plane for the i^{th} class. One-dimensional membership functions generally have asymmetric trapezoidal shape with maximal value of 1 and minimal value of 0 (Fig. 1).

These trapezoidal functions are described by 4 parameters: x1, x2, x3, and x4 as shown in Fig. 1.

[1] The distributions are similar to probability distributions, but are not normalized.

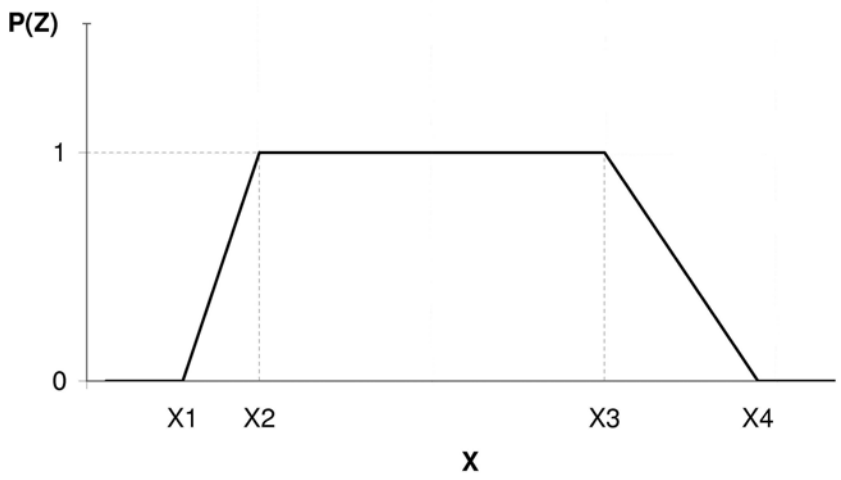

Fig. 1: Trapezoidal membership function

Aggregation value for each class is defined as:

$$Q_i = \sum_{j=1}^{M} W_j \, F^{(j)}(Z, V_j), \tag{3}$$

where W_j is the weight assigned to the j^{th} variable and M is the number of variables. Hydrometeor class is identified by the maximal aggregation value.

In our classification analysis, we use both Eq. (1) and (2) to determine the membership functions $F^{(i)}$. The choice of Eq. (2) is preferable if the distribution of the variable V_j strongly depends on the radar reflectivity as a parameter. This is usually the case for differential reflectivity Z_{DR} in rain, i.e., Z_{DR} increases with increasing Z.

Five radar variables have been used for automatic classification so far. These are: (1) radar reflectivity Z, (2) differential reflectivity Z_{DR}, (3) cross-correlation coefficient ρ_{hv} between horizontally and vertically polarized components of the radar return, (4) a texture parameter SD(Z) of the Z field, and (5) a texture parameter SD(Φ_{DP}) of the field of differential phase Φ_{DP}. The two latter variables are especially efficient for discrimination between meteorological and non-meteorological radar echoes. The parameters SD(Z) and SD(Φ_{DP}) characterize the intensity of small-scale fluctuations of Z and Φ_{DP} along the radar ray. To obtain SD(Z), we average Z data (sampled every 0.256 km) along the radial using 1-km-width running average window and subtract the smoothed estimates of Z from their original values. A similar procedure is used for computing the parameter SD(Φ_{DP}), but with an averaging window that is two times larger.

Two polarimetric variables, Z_{DR} and ρ_{hv}, are smoothed along the radial using a fivr point averaging interval. Both Z_{DR} and ρ_{hv} should be corrected for noise prior to application of the classification algorithm. This is especially important for light rain, snow, and clear-air echoes caused by biological scatterers. Z_{DR} and ρ_{hv} are noticeably biased if signal-to-noise ratio (SNR) is less than 20 dB. Efficient correction of both variables can be made for SNR > 5 dB. If SNR < 5 dB, then correction is considered unreliable and no classification is performed.

Because the Sigmet RVP7 processor does not provide SNR directly, we estimate SNR from radar reflectivity factor Z and distance R using the following formula

$$\mathrm{SNR\ (dB)} = \mathrm{Z(dBZ)} - 20\log(\mathrm{R(km)}) + \mathrm{C}, \qquad (4)$$

where the "constant" C is usually between 27 and 33. The value of C for a particular day of observations can be estimated using the scatterplots $\rho_{hv}^{(cor)}$ – SNR, where $\rho_{hv}^{(cor)}$ is the value of the cross-correlation coefficient corrected for noise as

$$\rho_{hv}^{(cor)} = \rho_{hv}\,(1 + 1/\mathrm{snr})\,. \qquad (5)$$

In (5) $\mathrm{snr} = 10^{0.1\ \mathrm{SNR\ (dB)}}$. If the constant C is estimated correctly, then the scatterplot $\rho_{hv}^{(cor)}$ – SNR is "flat" , i.e., there is no apparent dependence of $\rho_{hv}^{(cor)}$ on SNR for SNR > 5 dB. Such tuning of the constant C is performed automatically during data processing. Correction of Z_{DR} for noise is made according to the formula

$$Z_{DR}^{(cor)}(\mathrm{dB}) = 10\log[(\alpha\ \mathrm{snr}\ Z_{dr})/(\alpha\ \mathrm{snr} + \alpha - Z_{dr})], \qquad (6)$$

where $Z_{dr} = 10^{\ 0.1\ \mathrm{ZDR(dB)}}$ and α is a ratio of noises in the horizontal and vertical channels. In the current version of the classification algorithm, $\alpha = 1.48$ and $10\log(\alpha) = Z_{DR}^{(noise)} = 1.7$ dB.

The classification procedure can be customized according to the user needs. Different sets of radar variables, different classes, and different weight vectors **W** can be used in the classification routine. For example, the algorithm can be optimized either for discrimination between meteorological and non-meteorological scatterers ("meteo" versus "non-meteo") or for distinguishing different categories of meteorological echo (e.g., rain versus hail or snow).

At the moment, we use three different versions of the polarimetric classification algorithm with different degree of sophistication. Classification is performed with the data collected at one or two lowest elevations (0.5º and 1.5º). The same classification principles can be applied to the data obtained in vertical cross-section. However, since the RHI antenna scanning is not accepted in the NEXRAD mode of operation, the identification of radar echoes at two lowest PPI scans was our primary task during JPOLE.

2.1 Version 1: Meteorological versus non-meteorological scatterers

Version 1 represents the simplest type of the classification algorithm. It proves to be very efficient at discriminating between radar echoes caused by meteorological and non-meteorological scatterers such as ground clutter / anomalous propagation (AP), insects, birds, bats, and chaff. Three classes are identified according to this classification scheme: (1) hydrometeors of meteorological origin, (2) ground clutter / AP, and (3) non-meteorological scatterers in the atmosphere (insects, birds, bats, and chaff). All five radar variables are used for identification. The parameters x1 – x4 describing five one-dimensional membership functions for three classes are presented in Table 1. These functions are also displayed graphically in Fig. 2.

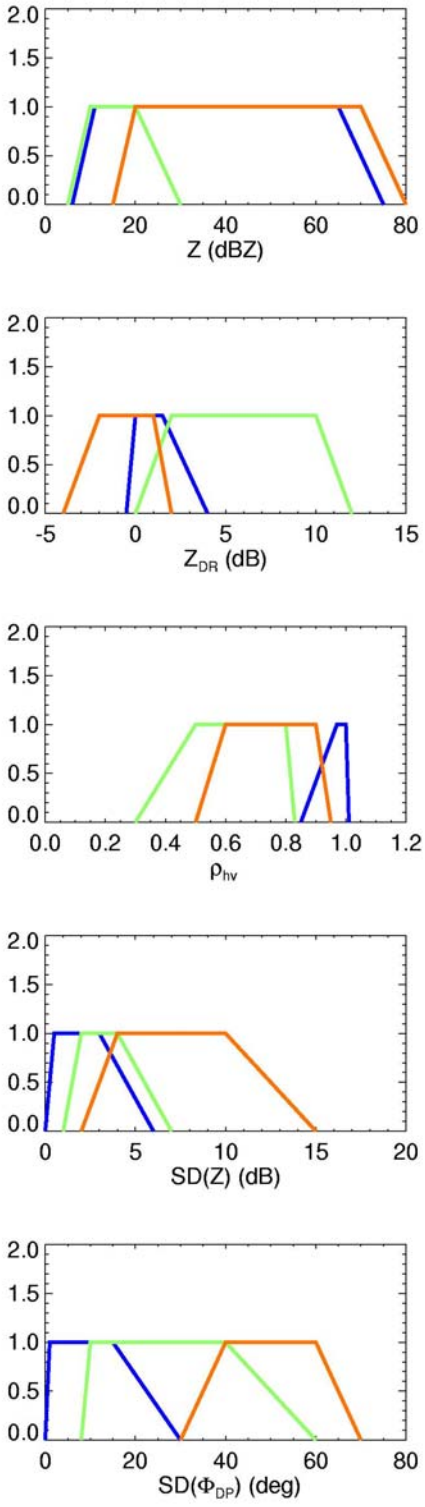

Fig. 2: Membership functions characterizing three classes: (1) meteorological scatterers (blue lines), (2) biological scatterers (green lines), and (3) ground clutter / anomalous propagation (red lines) with 5 radar variables.

Table 1: Membership function parameters for three classes.

P(Z)			
	GC/AP	BS	MS
x1 (dB)	15	5	5
x2 (dB)	20	10	10
x3 (dB)	70	20	65
x4 (dB)	80	30	75
$P_Z(Z_{DR})$			
x1 (dB)	-4	0	fl-0.3
x2 (dB)	-2	2	fl
x3 (dB)	1	10	fh
x4 (dB)	2	12	fh+0.3
$P(\rho_{hv})$			
x1	0.5	0.3	0.85
x2	0.6	0.5	0.97
x3	0.9	0.8	1.0
x4	0.95	0.83	1.01
P(SD(Z))			
x1 (dB)	2	1	0
x2 (dB)	4	2	0.5
x3 (dB)	10	4	3
x4 (dB)	15	7	6
$P(SD(\Phi_{DP}))$			
x1 (deg)	30	8	0
x2 (deg)	40	10	1
x3 (deg)	50	40	15
x4 (deg)	60	60	30

In Table 1, GC/AP stands for ground clutter / anomalous propagation, BS for biological scatterers, and MS for meteorological scatterers; fl and fh are functions of radar reflectivity

$$fl = -0.50 + 2.50\ 10^{-3}\ Z + 7.50\ 10^{-4}\ Z^2 \quad (7)$$

$$fh = 0.08 + 3.64\ 10^{-2}\ Z + 3.57\ 10^{-4}\ Z^2, \quad (8)$$

where Z is expressed in dBZ. One-dimensional membership functions $F^{(i)}(V_j)$ as defined by Eq. (1) are used for all variables and classes. The only exception is made for the membership function $F(Z,Z_{DR})$ of the meteorological scatterers, which is defined according to (2). Equal weights are given to all five radar variables in Eq. (3).

2.2 Version 2: The "summer" classification algorithm

Version 2 of the classification algorithm enables discrimination between radar echoes caused by (1) ground clutter and AP, (2) biological scatterers, (3) "big drops", (4) light rain, (5) moderate rain, (6) heavy rain, and (7) rain / hail mixture. In this algorithm, the term "big drops" is used to describe a raindrop spectrum that is characterized by a relatively larger number of big drops and fewer small drops than encountered in most DSDs. This skewed type of drop size distribution (DSD), which is commonly observed in zones of rapidly developing convection, has

important prognostic value for weather forecasters. Three radar variables: Z, Z_{DR}, and ρ_{hv} are used for classification. Historically, this is the earliest version of the classification algorithm. Several examples of classification using this algorithm are presented in section 4. Two texture variables, SD(Z) and SD(Φ_{DP}), will be added to a later version of the algorithm.

The two-dimensional membership functions $F^{(i)}(Z,V_j)$ determined from (2) are used in this version of the classification algorithm. The parameters of the membership functions for all 7 classes are presented in Table 2.

Table 2: Membership function parameters for the seven classes in the "summer" classification algorithm.

P(Z)							
	GC/AP	BS	BD	LR	MR	HR	R/H
x1 (dB)	25	5	15	5	30	40	45
x2 (dB)	35	15	20	10	35	45	50
x3 (dB)	75	20	45	35	45	55	75
x4 (dB)	85	30	50	40	50	60	80
$P_Z(Z_{DR})$							
x1 (dB)	-5	1	fh-0.3	fl-0.3	fl-0.3	fl-0.3	-0.3
x2 (dB)	-3	3	fh	fl	fl	fl	0
x3 (dB)	0	7	fb	fh	fh	fh	fl
x4 (dB)	2	9	fb+0.3	fh+0.3	fh+0.3	fh+0.3	fl+0.3
$P_Z(\rho_{hv})$							
x1	0.45	0.45	0.89	0.89	0.89	0.89	0.84
x2	0.55	0.55	0.90	0.90	0.90	0.90	0.85
x3	0.80	0.80	1.00	1.00	1.00	1.00	0.96
x4	0.90	0.90	1.01	1.01	1.01	1.01	0.97

In Table 2, GC/AP stands for ground clutter / anomalous propagation, BS for biological scatterers, BD for big drops, LR for light rain, MR for moderate rain, HR for heavy rain, R/H for rain/hail mixture; fl and fh are defined by (7) and (8); fb is another function of radar reflectivity given by:

$$fb = - 0.20 + 0.108\, Z - 6.43\, 10^{-4}\, Z^2, \qquad (9)$$

where Z is expressed in dBZ. Equal weights $W_1 = 1$ and $W_2 = 1$ are given to the membership functions associated with Z_{DR} and ρ_{hv} in Eq. (3).

Note that some parameters of similar membership functions in Table 1 and Table 2 are different because the classification procedure continuously evolved during the JPOLE period. Therefore, earlier and later versions of the classification algorithm differ in details. For each classification example in this report, we clearly specify the version of the classification algorithm used.

2.3 Version 3: The "winter" classification algorithm

In the version of the classification algorithm that is used for cold season weather events, we added two categories of snow particles, dry and wet snow, to the list of classes. This version of the algorithm uses Z, Z_{DR}, and ρ_{hv}, along with the texture parameter of the Z field SD(Z), to perform classification. It enables discrimination between radar echoes caused by (1) ground clutter and anomalous propagation, (2) biological scatterers (including insects and birds), (3) dry snow, (4) wet snow, (5) stratiform rain, (6) convective rain, and (7) rain/hail mixture.

Table 3 contains parameters of the membership functions for the "winter" classification algorithm. As in version 2, the two-dimensional membership functions defined from (2) are utilized.

Table 3: Membership function parameters for the seven classes in the "winter" classification algorithm.

P(Z)							
	GC/AP	BS	DS	WS	SR	CR	R/H
x1 (dB)	25	5	5	15	5	38	48
x2 (dB)	35	15	10	25	10	43	53
x3 (dB)	75	20	25	35	43	53	75
x4 (dB)	85	30	30	45	48	58	80
$P_Z(Z_{DR})$							
x1 (dB)	-5	0	-0.3	0.6	fl-0.3	fl-0.3	-0.3
x2 (dB)	-3	3	0	1.0	fl	fl	0.0
x3 (dB)	0	7	0.3	1.8	fb	fb	fl
x4 (dB)	2	10	0.6	2.2	fb+0.3	fb+0.3	fl+0.3
$P_Z(\rho_{hv})$							
x1	0.45	0.45	0.93	0.83	0.97	0.96	0.84
x2	0.55	0.55	0.94	0.85	0.98	0.97	0.85
x3	0.70	0.70	0.97	0.94	1.00	1.00	0.96
x4	0.80	0.80	0.98	0.96	1.01	1.01	0.97
$P_Z(SD(Z))$							
x1 (dB)	4	1	-0.5	0	-0.5	-0.5	-0.5
x2 (dB)	6	2	0.5	1	0.5	0.5	0.5
x3 (dB)	30	4	3	3	2.5	2	2
x4 (dB)	32	5	4	4	3.5	3	3

In Table 3, GC/AP stands for ground clutter / anomalous propagation, BS for biological scatterers, DS for dry snow, WS for wet snow, SR for stratiform rain, CR for convective rain, and R/H for rain / hail mixture; functions fl(Z) and fb(Z) are defined by Eq. (7) and (9).

Several classes of radar scatterers have very distinctive polarimetric properties. Because of this, they can be easily recognized if the fuzzy logic methodology is applied on a pixel-by-pixel basis. This means that no analysis of general pattern or surrounding pixels is needed. Ground clutter / AP, insects, birds, chaff, hail, wet snow (bright band) belong to this category of scatterers. All are characterized by anomalously low values of cross-correlation coefficient. Differential reflectivity is mainly negative for ground clutter / AP, very high positive for biological scatterers and chaff, and moderately high for wet snow. A combination of high Z and

relatively low Z_{DR} is a distinctive feature of hail or rain/hail mixture. SD(Z) is usually much higher for non-meteorological scatterers (especially for ground radar returns) than for any weather hydrometeors.

Discrimination between stratiform rain and dry aggregated snow is a major problem because membership functions in the fuzzy logic formalism heavily overlap. Both classes are characterized by relatively low Z and Z_{DR} combined with high ρ_{hv} (Ryzhkov and Zrnic 1998). Furthermore, there is no distinction in terms of the texture of the Z field as well.

Fig. 3 illustrates three scatterplots of Z versus Z_{DR} obtained from the measurements with the KOUN radar for three different types of snow. Dry aggregated snow was observed over the entire state of Oklahoma between 15 and 16 UTC on 6 February 2003. Seven hours later, the dry aggregated snow changed over to more crystallized snow in the very cold air NW of the radar. This snow was characterized by a much higher Z_{DR} and a lower Z. Heavy convective snowfall occurred on 24 February 2003 in southern Oklahoma. The corresponding Z – Z_{DR} scatterplot for the period between 22 and 24 UTC is also displayed in Fig. 3. Radar reflectivities over 50 dBZ are unusually high for snow in the latter case, but corresponding values of Z_{DR} are relatively low compared to those typically observed at the bottom of the radar bright band. The region between the two curves in Fig. 3 represents locations of Z – Z_{DR} pairs for pure rain as derived form the multi-year statistics of DSD measurements in central Oklahoma.

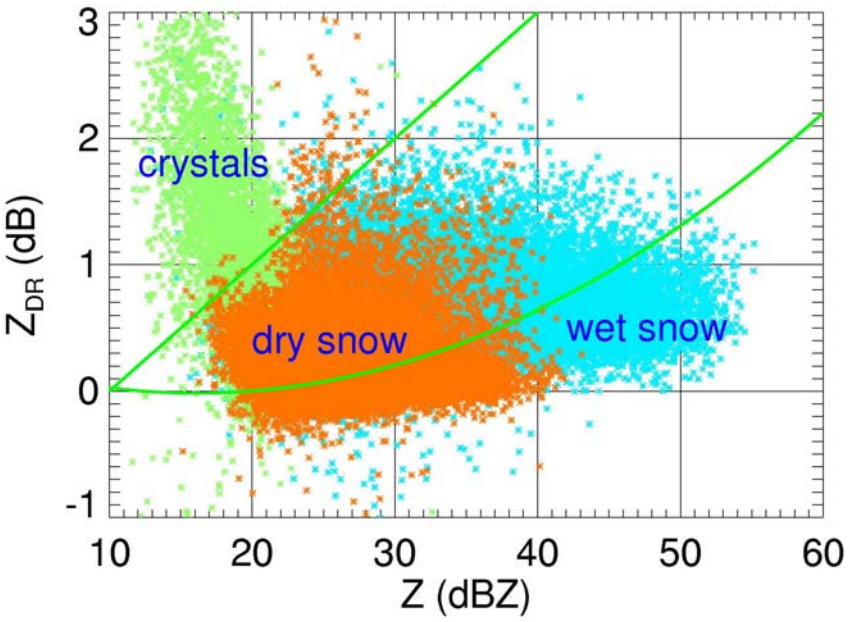

Fig. 3: Z – Z_{DR} scatterplots for different types of snow. The two curves confine the "rain" area.

It is evident that data from rain and snow heavily overlap in the $Z - Z_{DR}$ plane for reflectivities between 20 and 40 dBZ. There is no clear distinction between these two classes in K_{DP} and ρ_{hv} as well. A clue for successful discrimination between these classes lies in the fact that stratiform rain and aggregated snow are usually separated by the bright band, which has very pronounced polarimetric signatures and can be easily detected. Therefore, rain / snow delineation is contingent upon the reliable identification of the radar bright band.

Although it is easier to perform bright band identification with RHIs, we have to do classification with PPIs because RHI antenna scanning is not accepted in the NEXRAD mode of operations. Figs. 4 and 5 exhibit the melting level in the fields of Z, Z_{DR}, and ρ_{hv} at two lowest elevation tilts: 0.5 and 1.5° in the case of a stratiform rain with relatively low bright band.

At both elevations, radar reflectivity gives little clue about the location and height of the melting level. The bright band signature is more pronounced in the Z_{DR} field, particularly at higher elevations. However, the best indication of the melting level is given by ρ_{hv} at 1.5°, where the cross-correlation coefficient drops abruptly from 0.99 to less than 0.96 at the slant range where a radar beam intersects the bottom of the melting layer. After dropping in the melting layer, ρ_{hv} tends to increase in dry snow aloft. This increase, however, might be masked with a general decrease of ρ_{hv} with range due to weakening of radar signal and broadening of the radar beam. It can be shown that ρ_{hv} is negatively biased if signal-to-noise ratio is less than 20 dB. The same is true for Z_{DR}. Thus, an appropriate correction of ρ_{hv} and Z_{DR} at low SNR is crucial for rain / snow discrimination.

In the current version of the classification algorithm, slant ranges separating rain and melting snow are determined at every azimuth from the radial profiles of corrected ρ_{hv} at the elevation of 1.5°. After some editing and median filtering in azimuth, the "bright band contour" is generated at 1.5°. The corresponding "bright band contour" at lower elevations is obtained from the one at 1.5° using simple geometric considerations and an assumption of horizontal uniformity. The traditional "fuzzy logic" approach using all available radar variables is then applied for classification on a pixel-by-pixel basis at both elevations. However, categories of rain and non-meteorological scatterers are prohibited beyond the "bright band contour" where snow is expected. Similarly, snow is not allowed to appear below bright band. The bottom panel of Fig. 5 represents results of rain / snow discrimination for the case of 10/24/02. Application of this algorithm to a winter storm event is presented in section 4.4.

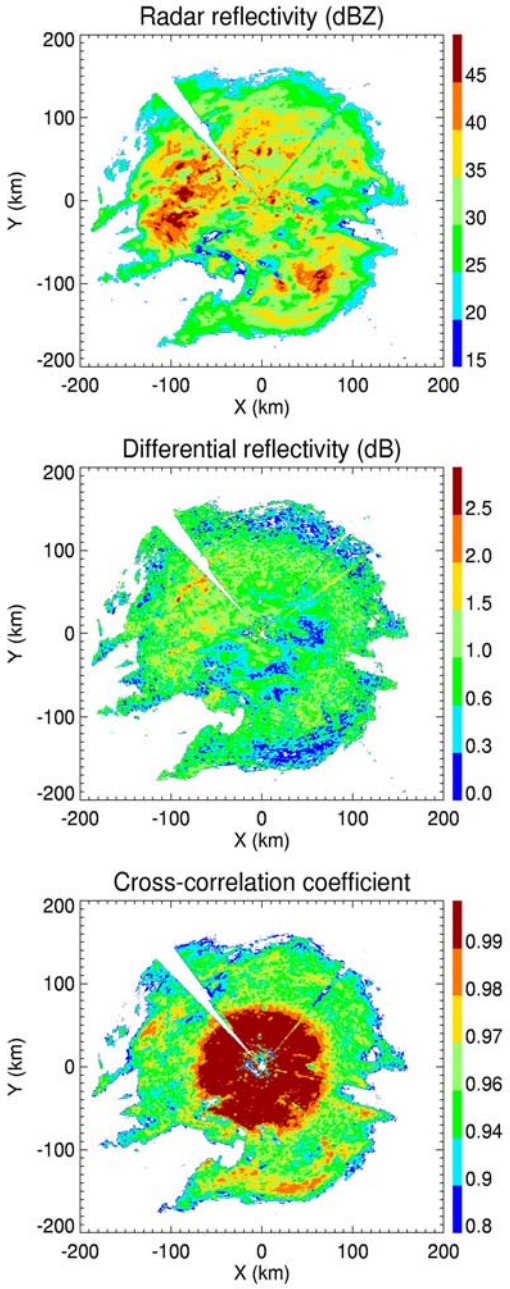

Fig. 4: Composite plot of Z, Z_{DR}, and ρ_{hv} at El = 1.5º for stratiform rain on 24 October 2002 (1832 UTC).

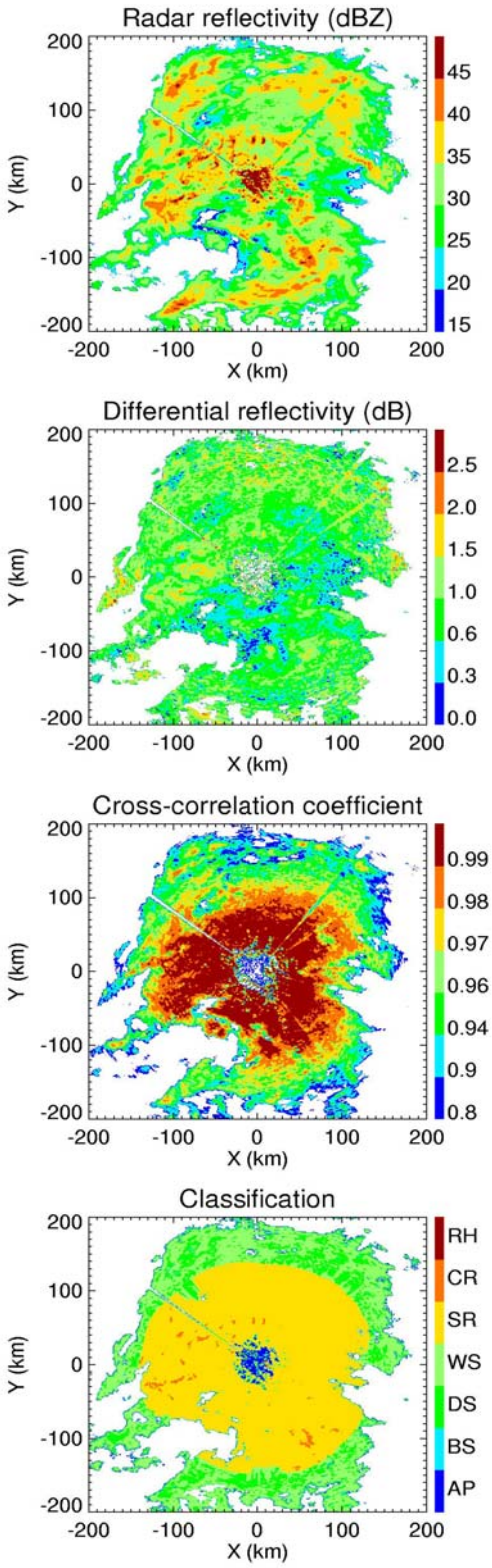

Fig. 5: Composite plot of Z, Z_{DR}, ρ_{hv}, and results of classification at El = 0.5º for stratiform rain on 24 October 2002 (1832 UTC).

3. Improvement in data quality

There are several data quality issues that can be addressed with polarimetric radar. Here we list three methods where the large JPOLE dataset is used to demonstrate the following data quality improvements: 1) filtering out non-meteorological echoes, 2) improving the accuracy of radar reflectivity measurements, and 3) using information on biological scatterers to improve the retrieval of Doppler winds in clear air.

3.1 Filtering out non-meteorological echoes

In most weather-related applications, users prefer to work with fields of radar variables that are not contaminated with echoes of non-meteorological origin such as ground clutter / AP, insects, birds, bats, and chaff. Meteorological and non-meteorological scatterers possess very distinctive polarimetric properties. A detailed description of polarimetric contrasts between weather and non-weather radar echoes, along with several supporting examples, is given in section 4.5.

In order to assess the ability of the KOUN radar to classify meteorological and non-meteorological scatterers, we have selected 8 cases that exhibited extensive areas of radar echo caused by either AP or biological scatterers. A list of these cases is presented in Table 4 Additional information about the selected cases can be found at http://cimms.ou.edu/~heinsel/jpole/database.html and http://cimms.ou.edu/~heinsel/jpole/stormtype.html.

Table 4: List of the JPOLE cases with the most pronounced non-meteorological echoes.

Number	Date	Time (UTC)	Description
1	06/13/2002	3 - 9	AP in the rear side of MCS
2	08/13/2002	9 - 11	AP and Bio mixed with rain
3	08/24/2002	6 - 9	AP and Bio mixed with rain
4	08/28/2002	11 - 14	Widespread AP, no rain
5	09/15/2002	1 - 8	Migratory birds and rain
6	10/27/2002	2 - 9	Migratory birds and rain
7	10/29/2002	5 - 13	Migratory birds and light rain
8	05/01/2003	9 - 12	Very strong and extended AP

For each case using the version 1 of the classification algorithm, we perform echo classification every 6 to 15 minutes at the two lowest elevation tilts, 0.5º and 1.5º. Three classes of radar echo: hydrometeors, biological scatterers, and ground clutter / AP are distinguished. The radar data and results of classification for both elevations are then displayed and stored for the 400 x 400 km area in Cartesian format with a grid resolution 2 x 2 km. For each event, we examined animations of the fields of classified echoes to check spatial and temporal continuity of the classification results. This visual continuity test shows good spatial and temporal "coherency" of the classification fields with a consistency that one would expect from common sense.

To our knowledge, there is no well established methodology for quantitative assessment of the performance of such classification procedures. Because of lack of verification data at such small spatial and temporal scale, accurate ground truth validation is not possible. Rain gage

information can be useful only to determine whether rain is falling in close proximity of the gage. Satellite data analysis is another option to assess the possibility of rain or AP over large areas (but with more coarse spatial and temporal resolutions). Validation information regarding biological scatterers and their flying habits is also very limited. In some previous studies (e.g., Moszkovicz et al. 1994) an "assessment of well-trained radar operator" was used as a ground truth to validate different techniques for AP detection and mitigation. This criterion is quite subjective and, unfortunately, there is no simple way to avoid a certain degree of subjectivity for such a validation. Our approach to validate the ability of the classification scheme to recognize meteorological and non-meteorological echoes is also not entirely void of subjectivity.

We select areas of the radar echo at both elevation tilts which should contain only weather or non-weather echoes and count the number of 2 x 2 km pixels identified as "meteo" or "non-meteo". Distances in close proximity to the radar and areas where a complex mixture of the echoes from AP, biological, and meteorological scatterers are present have been avoided. We have identified such "test" areas for all events listed in Table 4 and examined multi-hour statistics of classification for each of these areas. The number of pixels identified as "non-meteo" in pure rain areas was usually less than 1% of the total number of pixels for which SNR > 10 dB. A similar proportion of misclassification (less than 1 %) was found in an opposite situation - "meteo" pixels in the AP areas - provided that SNR is again higher than 10 dB. The quality of classification deteriorates with decreasing SNR (up to 5% of misclassified pixels in several cases if SNR > 5 dB). This deterioration is attributed to the fact that the key polarimetric variables Z_{DR} and ρ_{hv} are biased by noise and their reliable correction is possible if SNR > 5 – 10 dB. The use of total differential phase Φ_{DP} which is not affected by noise is more promising at relatively weak signals. This option will be carefully explored in the near future. The major problem, however, will be the separation of the contributions from the forward scattering and backscattering effects in the total differential phase. Only the "backscattering portion" of Φ_{DP} should be used for classification.

3.2 The accuracy of radar reflectivity measurements

Once the sources of radar echo are identified and "unwanted" echoes are filtered out, the next problem is to ensure high accuracy of the radar reflectivity measurements. The radar reflectivity factor Z can be biased due to radar miscalibration, partial beam blockage, and attenuation in rain and hail. The latter factor has usually been ignored at S band. Ryzhkov and Zrnic (1995) showed that, for extended regions of heavy precipitation typical for Great Plains, the Z bias due to attenuation can be significant. It was shown, that in pure rain (without hail) such bias at S band can be approximately estimated from Φ_{DP}:

$$\Delta Z \text{ (dB)} = 0.04\ \Phi_{DP} \text{ (deg)} \qquad (10)$$

Those observational results were supported by theoretical simulations by Bringi et al. (1990). Measured differential phases exceeding 100º are very common for precipitation in Oklahoma. This means that negative biases of Z over 4 dB in magnitude occur quite frequently at long propagation paths in precipitation. Such biases cause about two times underestimation of rain rate if the conventional NEXRAD relation is utilized and poor hail detection at large distances from the radar. An example of significant attenuation along a squall line is presented in Fig. 6. In this example differential phase exceeds 250º in the western part of a squall line and the corresponding bias of Z is larger than 10 dB! A gradual decrease of Z with range along the squall line is quite obvious in Fig. 6a. As a result, hail at large distances from the radar is not identified. The problem is fixed if radar reflectivity is corrected according to Eq. (10) (Fig. 6b). Attenuation

in hail is much more significant than in rain and the coefficient of proportionality in (10) is even higher in the presence of hail along the propagation path.

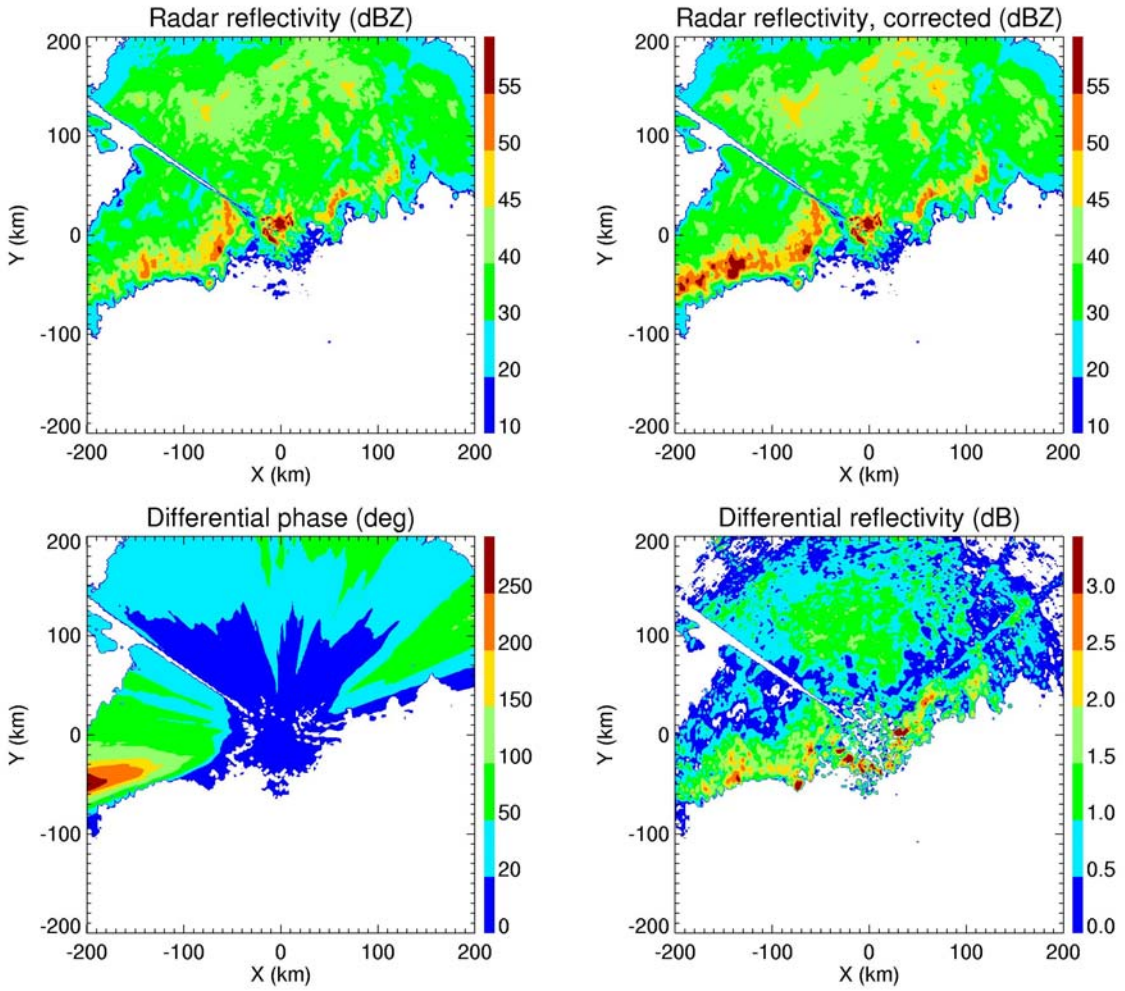

Fig. 6: Radar reflectivity measured and corrected (for attenuation) and measured fields of differential reflectivity and differential phase. 16 June 2002, 0201 UTC, El = 0.5º

Accurate calibration of the radar reflectivity factor still remains a serious problem in the WSR-88D radar network. Recent findings by Gourley et al. (2003) show that Z biases of 2 – 3 dB are quite common. The problem of accurate measurements of Z is further exacerbated at the lowest elevations where a radar beam can be partially blocked. One of the great advantages of a polatimetric radar is its ability to measure specific differential phase K_{DP}, which is immune to radar system miscalibration, beam blockage, and attenuation in precipitation. Goddard et al. (1994) and Gorgucci et al. (1999) suggested a self-consistency check using Z, Z_{DR}, and K_{DP} to assess possible biases in Z. According to this approach, Z, Z_{DR}, and K_{DP} are not independent variables in rain, and Z at horizontal polarization can be roughly estimated from Z_{DR} and K_{DP} using the following relation

$$Z = a + b \log(K_{DP}) + c\, Z_{DR}\,, \qquad (11)$$

where Z is expressed in dBZ, Z_{DR} - in dB, and K_{DP} – in deg/km. The coefficients a, b, and c in (11) depend on a radar wavelength and are relatively insensitive to the drop size distribution

(DSD) variations. We used the multiyear statistics of DSDs in central Oklahoma measured with the 2D-video disdrometer to compute radar variables at the wavelength of 11 cm and obtained the following coefficients: a = 48.5, b = 11.4, and c = 0.94. In a companion report (Ryzhkov et al. 2003), we examine the performance of the polarimetric consistency technique for radar reflectivity calibration via direct comparisons of reflectivities measured by the KOUN radar and operational KTLX radar located at the distance of 20.3 km from the polarimetric one. For 19 rain events (out of total 22 examined) the difference between two estimates (polarimetric and direct) was within 1 – 1.5 dB. We believe that, after some additional refinements, the polarimetric consistency technique will provide the accuracy of the radar reflectivity measurements within 1 dB.

Specific differential phase K_{DP} does not require calibration, whereas differential reflectivity Z_{DR} does. However, since Z_{DR} is a relative parameter (a ratio), it is easier to calibrate Z_{DR} than Z. As shown by Melnikov et al. (2003), the bias of Z_{DR} was kept under 0.2 dB for the KOUN measurements during JPOLE. According to the consistency relation (11), the Z_{DR} measurement error of 0.2 dB causes the corresponding error of Z calibration less than 0.2 dB. Differential reflectivity measurements can be biased more significantly if the radar beam at lowest elevation is partially blocked (Ryzhkov et al. 2002a). This is the case for the NSSL's research Cimarron polarimetric radar. Ryzhkov et al. (2002a) have developed a methodology for the calibration of Z_{DR} in the presence of severe beam blockage. After Z_{DR} is properly calibrated, Eq. (11) can be applied to obtain an unbiased radar reflectivity factor even in the case of substantial blockage of the radar beam.

3.3 Doppler wind measurements in clear air

All methods for Doppler wind measurements in clear atmosphere assume that clear-air radar scatterers are ideal tracers of wind and turbulence, i.e., they do not have their own component of motion. Biological scatterers like insects, birds, and bats represent the overwhelming majority of the clear-air scatterers (along with small-scale nonuniformities of refractive index caused by turbulence). If these biological scatterers are strong flyers, they produce a bias in Doppler wind estimates that needs to be eliminated from meteorological analysis. It is important to distinguish between passive (mostly insects) and non-passive tracers of winds (birds and bats) in order to guarantee acceptable quality of radar wind retrievals in clear atmosphere such as VAD (Velocity – Azimuth Display). It is very common that the VAD wind profiles obtained during peaks of nocturnal bird migration in spring and fall are heavily contaminated. Zrnic and Ryzhkov (1998) were the first who showed significant differences in polarimetric properties of small Rayleigh scatterers like insects and big non-Rayleigh scatterers like birds. Birds usually have much larger differential phase upon scattering δ and lower differential reflectivity Z_{DR} than insects.

At the moment, all versions of our classification algorithm do not make a distinction between insects and birds; both are combined into the same "biological scatterers" class. One of the reasons for that is that polarimetric signatures of birds and insects have very pronounced azimuthal dependence and at certain azimuths (usually close to the main wind direction) Z_{DR} and δ for birds and insects are very similar. Therefore, their discrimination based on pixel-to-pixel fuzzy logic approach might not be efficient at these azimuthal directions. Nevertheless, there are extended areas of radar echo where such classification can be performed in very clear and straightforward way. In other words, the areas of high δ (of the order of 70 - 100º) and relatively small Z_{DR} (usually lower than 3 dB) associated with birds can be easily identified and the corresponding sectors of wind fields retrieved using the VAD technique should be censored.

Section 4.5 contains more detailed description of polarimetric signatures of insects and birds as well as some graphical examples of the differences between them.

4. Hydrometeor classification

In this section, we present case examples that demonstrate data quality, analyses that demonstrate statistical improvement in hail detection capabilities, and discussion that summarizes the ability of polarimetric data to improve the identification of hydrometeor type within precipitation systems.

4.1 Tornadic Supercells

Previous research with the NSSL Cimarron radar (Ryzhkov et al. 2002b) led to the discovery of a polarimetric tornado signature associated with the Chickasha, OK airport F3 tornado of May 3, 1999 (note that a power failure associated with the initial touchdown of the larger and more destructive F5 Oklahoma City tornado on May 3, 1999 prevented collection of dual-polarization data for that tornado). The signature at the tip of the hook echo of that storm was detected by two polarization parameters: (1) differential reflectivity (Z_{DR}), which had a very low values around 0.0, and (2) cross-correlation coefficient (ρ_{hv}), which had anomalously low values of < 0.7 (and sometimes < 0.5). The Ryzhkov et al. (2002b) study concluded that the signature was associated with or attributed to non-meteorological scatterers that had an irregular shape and high refractive index (i.e., tornado debris). The signature was also found to have time continuity with tornado damage and height continuity (in the lower parts of the storm), as might be expected with the well-known tornado attribute of being able to loft debris.

As part of JPOLE, considerable KOUN data were acquired in tornadic storms. In particular, May was an active storm time with several damaging tornadoes near KOUN. Most notable were the afternoons and evenings of May 8, 2003 when a violent F4 tornado struck Moore, Southeast Oklahoma City, Midwest City, and Choctaw, OK (a 17 mile path length); and May 9, 2003 when a strong F3 tornado struck Northeast Oklahoma City, Witcher, and rural parts of Jones and Luther, OK (a 18 mile path length). In addition, 3 weak tornadoes (FO and F1) occurred within range of KOUN on May 8, 2003, and 9 weak tornadoes occurred within range of KOUN on May 9, 2003. KOUN tornadic storm data were also collected during lesser tornado events on April 19, April 23, May 6, the early morning of May 8, May 15, and May 16. We analyzed the JPOLE data with objectives of: (1) verifying the Z_{DR} and ρ_{hv} tornado debris signature, (2) better determining the uses and limitations of the signature, and (3) examining the dual-polarization data for the purpose of determining additional polarization tornado signatures. Examples of the polarimetric signatures associated with the May 8, 2003 and May 9, 2003 tornadic storms are shown below in Section 4.1.1.

4.1.1 Examples of KOUN data from a tornadic supercell

Figure 7 shows KOUN Z, Z_{DR}, K_{DP}, and ρ_{hv} for the May 8, 2003 tornadic supercell thunderstorm, which produced an F4 tornado over Moore and southern Oklahoma City, OK. In agreement with the results of Ryzhkov et al. (2002b), a distinct polarimetric signature, which consists of a low Z_{DR} and anomalously low ρ_{hv}, can be seen at a location of X=9 km, Y=18 km.

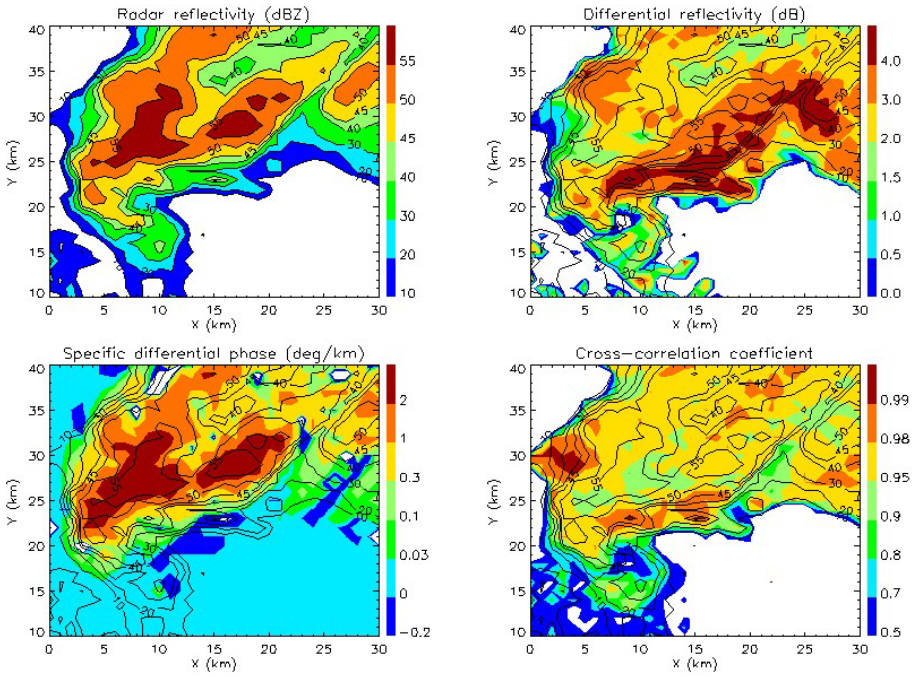

Fig. 7: Four panel image for the Moore/Southeast Oklahoma City tornado of May 8, 2003: (upper left) reflectivity, (upper right) differential reflectivity (Z_{DR}), (lower left) specific differential phase, and (lower right) cross-correlation coefficient (ρ_{hv}). Time is 2228 UTC on May 8, 2003. The tornado signature in Z_{DR} and ρ_{hv} is at the tip of the hook echo (X=9 km, Y=18 km).

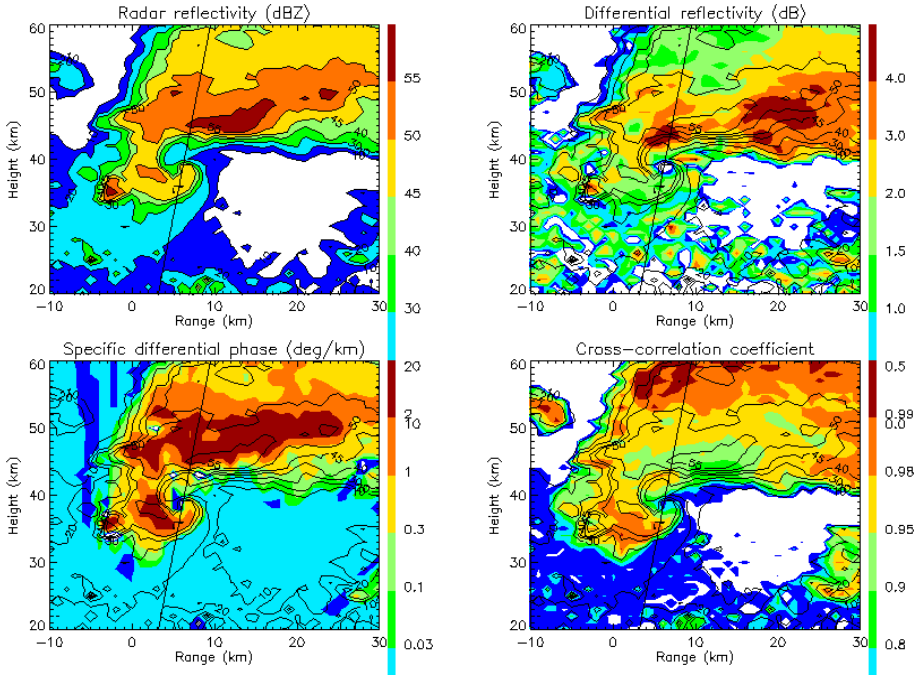

Fig. 8: Four panel image of the Northeast Oklahoma City tornado of May 9, 2003: (upper left) reflectivity, (upper right) differential reflectivity (Z_{DR}), (lower left) specific differential phase, and (lower right) cross-correlation coefficient (ρ_{hv}). Time is 0346 UTC on May 10, 2003. The tornado signature in Z_{DR} and ρ_{hv} is at the tip of the hook echo (X=7 km, Y=39 km). The line at 9° azimuth in all four panels indicates the location of the RHI depicted in Fig. 10.

This pattern is repeated for the May 9, 2003 tornadic supercell thunderstorm in Fig. 8, which shows a similar polarimetric signature in the KOUN Z, Z_{DR}, K_{DP}, and ρ_{hv} fields at a location of X=7 km, Y= 39 km for the storm that passed through northern Oklahoma City, OK.

During the spring of 2003 data collection, the "summer" classification algorithm (as discussed in section 2.2) was run on real-time data and delivered to operational forecasters at the Norman, OK NWS forecast office. This "summer" classification scheme does not contain a category for tornadic debris. Nevertheless, a tornadic signature that was classified as anomalous propagation (AP) was consistently identified for the duration of the tornado path, suggesting that it might be possible to add a tornadic debris classification category to future versions of the algorithm. Fig. 9, which shows the classification algorithm results for the KOUN Z, Z_{DR}, K_{DP}, and ρ_{hv} at 0346 UTC, May 10, 2003, also depicts this signature (tornado signature shown as AP at the tip of the hook echo).

Finally, we present vertical cross-sections of KOUN Z, Z_{DR}, K_{DP}, and ρ_{hv} through the May 9, 2003 supercell at 0346 UTC (Fig. 10). As with Fig. 8, the location of the tornado in these cross sections is clearly indicated in all four fields at a range of approximately 39 km. Fig. 10 also demonstrates the height continuity of the tornadic signature, which is seen to extend to a height of ~ 2.0 km in several of the fields, and provides indications of polarimetric signatures aloft that might be used, after additional research, to identify microphysical precursors to tornadogenesis.

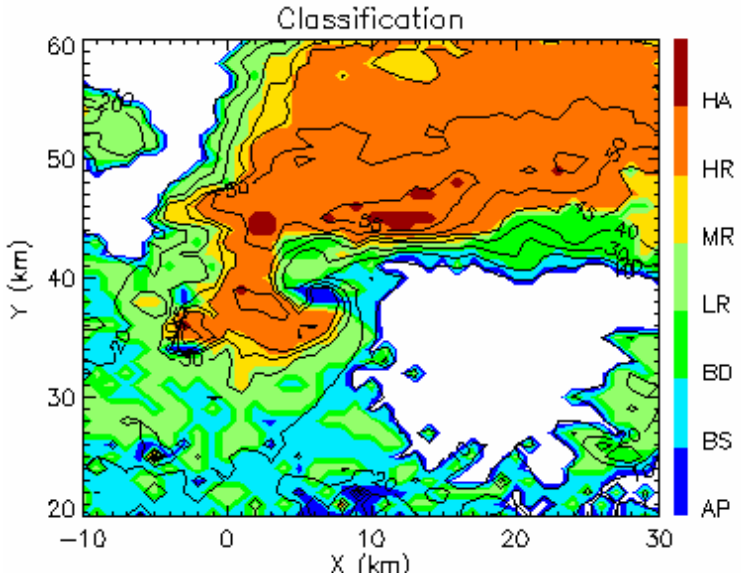

Fig. 9: Hydrometeor classification results of the May 9, 2003 tornadic supercell at 0346 UTC. Results are for an elevation of 0.5° (corresponding to the four data panels in Fig. 8).

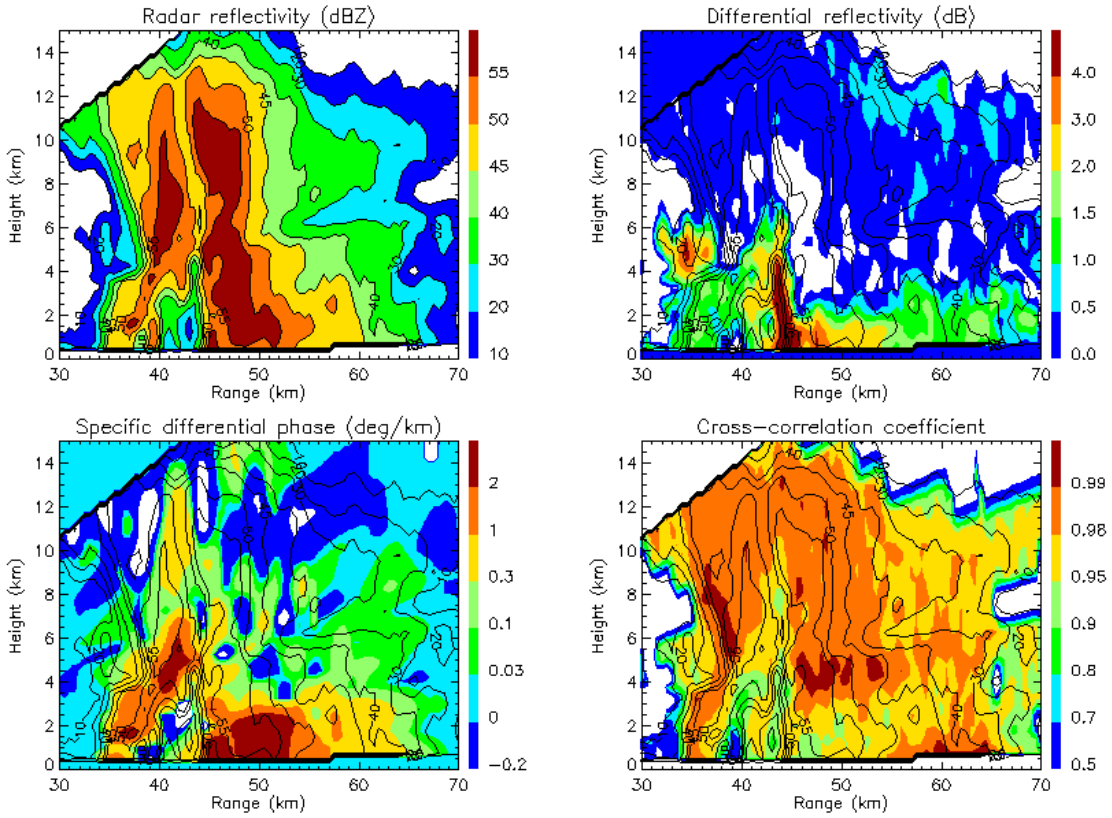

Fig. 10: Four panel RHI image of the Northeast Oklahoma City tornado of May 9, 2003: (upper left) reflectivity, (upper right) differential reflectivity (Z_{DR}), (lower left) specific differential phase, and (lower right) cross-correlation coefficient (ρ_{hv}). Time is 0346 UTC on May 10, 2003. RHI is at a 9° azimuth (depicted by the line in all four panels of Fig. 8). The tornado signature in located at a range of approximately 39 km.

4.1.2 Analysis results

The May 8, 2003 and May 9, 2003 datasets, shown above, were given priority for analysis. One limitation of the May 8, 2003 dataset is a data gap of 18 minutes during the F4 tornado. This gap was caused by a tornado-induced power failure when the tornado was in the western part of Moore (similar to the May 3, 1999 event discussed above). Data were, however, available for the first minute and the last 10 minutes of the tornado's life. On May 9, 2003, KOUN operated on generator power, and data were continuous. For both May 8, 2003 and May 9, 2003, volume coverage patterns (VCPs) consisted of 15 elevation angles (0.0 to 19.5 deg) collected in 5-6 minutes (the CONVECTIVE or TORNADO VCPs, see discussion in Schuur et al. 2003a).

After examination of the May 8, 2003 and May 9, 2003 datasets, several results can be stated:

1) The signature is reproducible. The May 3, 1999 type debris signature was very obvious for the strong tornadoes that struck areas with large numbers of structures (F4 on May 8 and F3 on May 9). Z_{DR} and ρ_{hv} values were also similar to May 3, 1999 and the horizontal and vertical extents of the signatures were comparable (horizontal size ~1 km and vertical extents of ~2-4 km).

2) A signature is not seen for all tornadoes. The majority of the weak tornadoes did not possess definable signatures. Some of the weak tornadoes were in urban areas where

many structures were located, while other weak tornadoes were in rural areas where few structures were located. One possible reason for the inability to detect a signature is that the weaker tornadoes (F0 and F1) did not possess winds speeds fast enough to significantly damage structures and loft debris. Another possible reason is that, because some of the weaker tornadoes only existed for a few minutes, a debris signature could have been missed because of the antenna being at VCP high elevation angles. However, at least two weak tornadoes did possess identifiable signatures.

3) Maximum signature detection ranges could not be determined. The two strongest tornadoes were at relatively close ranges (<60 km). More observations of tornadoes at medium ranges (100-150 km) need to be taken and examined. Weak tornadoes might not possess a signature at any range.

4) The ρ_{hv} parameter appears to have better signature discriminating power**.** Although both Z_{DR} and ρ_{hv} are useful for the debris signature *and should be used together to maximize signature detection probability*, ρ_{hv} appears to have the better signature discriminating power because its highly anomalous values are in the debris region. Z_{DR} values near 0.0 can occur with precipitation particles, allowing for some ambiguity between debris and normally occurring precipitation. On the other hand, ρ_{hv} values are confined to a smaller range for precipitation particles (usually > 0.9), meaning that debris values (~ 0.7 down to below 0.5) are more unique.

5) Other polarization tornado signatures (in addition to the debris signature) are possible, but could not be determined by this analysis. With supercell storms, the type and evolution of precipitation particles in the developing rear-flank downdraft and hook echo may play important roles in tornadogenesis and tornadogenesis failure. Unfortunately, such evolutions are complicated and require extensive analysis time that was not available. In the limited analysis that was done, no polarization parameter could be consistently linked to tornadogenesis in the tornadic supercells. Furthermore, no polarimetric parameter could identify tornadogenesis failure in the non-tornadic supercells. Study of non-tornadic supercells was limited to two storms on May 9, 2003 that preceded the multi-tornadic supercell. It still remains very possible that a polarization tornadogenesis signature exists, but it will take collection and analysis of additional data to find it.

4.1.3 Application of Results

Several comments can be made about the results to date:

1) *Utility of the polarization debris signature in NWS tornado warnings and other products:* The foreseen utility of the debris signature will mostly be in confirming previously existing tornado warnings. Tornado warnings for the May 8, 2003 F4 and May 9, 2003 F3 had already been issued before the debris signature was seen. Since it comes from debris, the signature has no lead time. In cases where traditional tornado-warning signatures are absent, not detected by radar, or overlooked by forecasters, *the polarization tornado signature will be very valuable in preventing what otherwise would have been missed important warnings.* Recent examples of such misses are Hall/White County, Georgia (1998), Salt Lake City, Utah (1999), Xenia, Ohio (2000), Hoisington, Kansas (2001), and La Plata, Maryland (2002). *The polarization tornado signature will also be very valuable in issuing accurate severe weather warning updates to pinpoint*

current tornado location and confirm occurrence of damage (based on debris). Warning updates are a current area of emphasis for the NWS and its partners (media, emergency managers, etc). It has been shown that a continuing flow of information greatly helps the warning process, and the debris signature will be an aid.

2) *Limitation of the polarization debris signature in NWS tornado warnings and other products:* The polarization debris signature will not be a source of information to conclude that a tornado is not occurring. Weak tornadoes (at any range from the radar) may not produce a debris signature. Because they haven't yet been studied, we can't say for sure that structure-damaging strong tornadoes at medium and longer ranges (>100 km) will have signatures. Also, no data has yet been collected on strong tornadoes in very rural areas where there are very few structures or other objects to be damaged and have debris lofted by the wind. Although unlikely, it's possible that a few strong tornadoes in very open areas may not loft enough debris to have definitive signatures.

3) *Need for further data collection and analysis:* The JPOLE experiment was very successful in the spring of 2003 in collecting several good tornadic storm datasets. However, there have not been enough resources (time or people) to completely analyze all of the data. Other datasets besides May 8, 2003 and 9, 2003 should be analyzed. Even if that is done, more data will need to be collected and analyzed to fully understand the debris signature, its utility and its limitations. A polarization precursor signature to tornadogenesis may be found with supercells, but its discovery, if found, will await further data collection and analysis. Finally, there is need to collect and analyze data for non-supercell tornadic storms. In particular, squall lines and bow echoes are known to produce large numbers of tornadoes, some of them strong tornadoes. Very little, if any, of the data already collected are from tornado-producing squall lines and bow echoes. Such cases occur frequently in Oklahoma within range of KOUN. Data should be collected on future events.

4.2 Hail

Another goal of JPOLE is to verify and document advantages of hail detection using the polarimetric Hydrometeor Classification Algorithm (HCA) compared to the non-polarimetric, operational hail detection algorithm (HDA) that is used by the NWS. As described previously, NSSL's polarimetric the HCA classifies hydrometeor type within each elevation scan. Therefore, when hail is present within a storm, we can pinpoint its location. Since our goal is to verify the algorithm's ability to identify the presence hail at the surface, we use HCA output at the 0.5° elevation. The operational the HDA (Witt et al. 1998) provides estimates of hail and severe hail probability, as well as maximum hail size, *anywhere* within a storm cell that is identified by the Storm Cell Identification and Tracking (SCIT) algorithm (Johnson et al. 1998). Since HCA currently only identifies the presence of hail, the probability of hail product is chosen for this algorithm comparison. The probability of hail is a function of the height of the 45-dBZ echo above the environmental melting level, such that higher probabilities of hail correspond with higher heights above the melting level (Witt et al. 1998). Thus, probability of hail forecasts by the HDA are founded on a physically-based empirical relationship, applicable to a storm cell, whereas classification of hail by the HCA is founded on characteristics of hydrometeors themselves, applicable to specific locations within a storm cell.

4.2.1 Example of KOUN data for a severe hail storm

During JPOLE, data were collected from 18 events that produced polarimetric signatures indicative of hail. Fig. 11 shows data collected during a severe hail storm that occurred over south-central, OK on May 14, 2003. Public reports indicated that hail with a diameter >13 cm had just fallen from the storm centered at approximately X= -10 km, Y= -85 km (the location of the 13 cm diameter hail report is indicated by the star in the four panels). Radar reflectivities in the hail core were > 65 dBZ. This was combined with very low and occasionally negative Z_{DR}s and very low ρ_{hv}s. The large regions of negative Z_{DR} and very low ρ_{hv} in this storm were undoubtedly due to severe differential attenuation. There were additional indications, especially at a lower elevation scan, that severe differential attenuation was impacting the results of the HCA. The HCA result for this case is shown in Fig. 12.

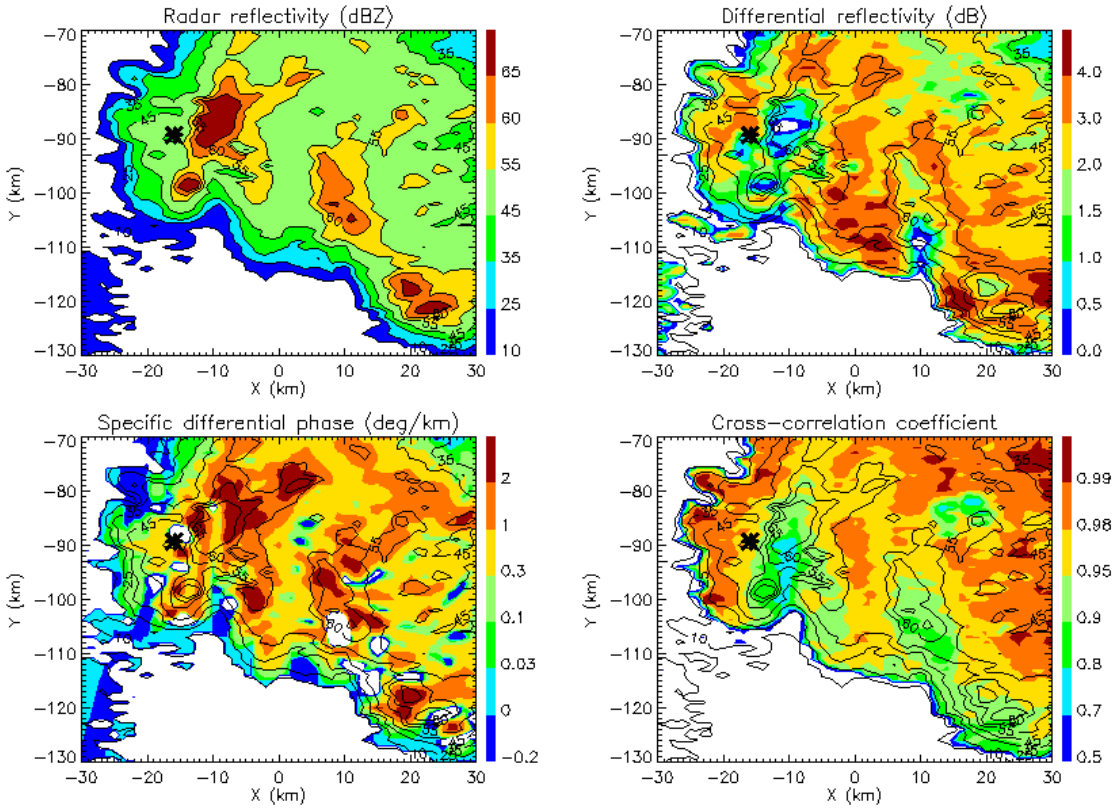

Fig. 11: Fields of polarimetric variables (PPI presentation) of the May 14, 2003 hail event at 0834 UTC. PPI is at 0.5° elevation. The panels display radar reflectivity (dBZ), differential reflectivity (dB), specific differential phase (°/km) and cross-correlation coefficient, respectively. The location of the 13 cm diameter hail report is indicated by the star.

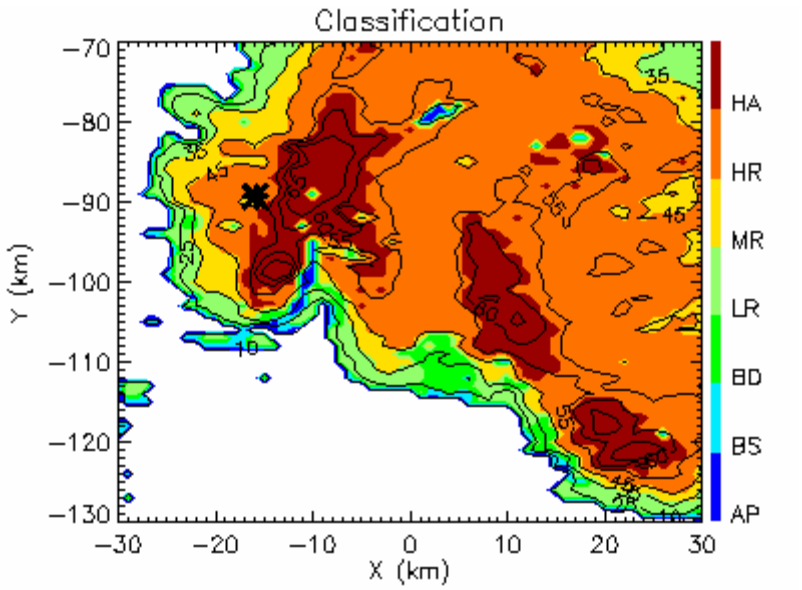

Fig. 12: Hydrometeor classification results of the May 14, 2003 hail event at 0834 UTC. Results are for an elevation of 0.5° (corresponding to the four data panels in Fig. 11). The location of the 13 cm diameter hail report is indicated by the star.

4.2.2 Verification methodology

During the project, two hail chase cars were deployed to intercept thunderstorm cores that had the potential to produce hail at the surface (Schuur et al. 2003a). The performance of the HCA and HDA is investigated by verifying their respective products against the ground truth dataset collected by those vehicles. This verification process begins by running each algorithm during periods comprising the ground truth. The HCA is run using data collected by the polarimetric KOUN radar, whereas the HDA is run using data collected by KTLX, a nearby operational WSR-88D radar. Unfortunately, data were only archived by both radars during 4 of the 5 events. The 11−12 June 2003, low-precipitation supercell case is therefore excluded from this comparison. The following rules are applied to verify algorithm products:

1) The product is considered for verification if the distance from the ground truth observations to the 40 dBZ contour and/or hail classification contour at the 0.5° tilt is within the storm's radius of influence, which varies from 3.2 to 5 km, depending on the speed of storm movement. Since HDA assigns a probability of hail to each storm cell, we assess the probability of hail associated with the cell located closest to the ground truth. Probabilities of hail 60% and higher are considered unambiguous "yes" forecasts of hail.
2) Products are compared to ground truth observations within a 12 minute window, centered at the time of the volume scan. This time window is chosen to reflect the maximum period between consecutive volume scans.
3) Given that criteria 1−2 are satisfied, a 2x2 contingency table is created for each day, and for all days combined.

The 2x2 contingency tables are used to quantify the accuracy and skill of the HCA and HDA, and are constructed by comparing algorithm detections to the ground truth observation. Within the contingency table (Table 5), *a* is a "hit", *b* is a "false alarm", *c* is a "miss", and *d* is a "correct null." In all, eight accuracy measures or conditional probabilities are computed for each

day, and for all days combined. By computing these statistics for each day, we can explore the relative sensitivity of algorithm performance to storm type. The eight conditional probabilities are given by: $P(F_{i=1,2},O_{i=1,2})$ and $P(O_{i=1,2},F_{i=1,2})$, where P is the conditional probability, F is the algorithm detection, O is ground truth, and the subscript i denotes either the presence (i=1) or absence (i=2) of hail in the algorithm detection and ground truth. Traditionally, only two of the eight conditional probabilities are examined in radar-based algorithm verification studies, including the probability of detection, $P(F_1,O_1)$, and the false alarm rate, $P(O_2,F_1)$ (Wilks 1995). In this study, all eight probabilities are calculated to construct a more complete understanding of forecast accuracy. The equations for these probabilities are given in Appendix A.

Table 5: Example of a 2x2 contingency table, where a is a "hit", b is a "false alarm", c is a "miss", and d is a "correct null."

	Hail Observed	**Hail Not Observed**
Hail detected by HCA or HDA	*a*	*b*
Hail not detected by HCA or HDA	*c*	*d*

For completeness, the Critical Success Index (Wilks 1995), $CSI = \frac{a}{a+b+c}$, and Hit Rate, $H = \frac{a+d}{n}$ are calculated as well, where *n* is the total number of observations. The skill of the HCA and HDA are quantified using the Heike skill score, $HSS = \frac{2(ad-bc)}{(a+c)(c+d)+(a+b)(b+d)}$, and the Kuipers skill score, $KSS = \frac{ad-bc}{(a+c)(b+d)}$ (Wilks 1995). Both the *HSS* and the *KSS* measure the "hit rate that would be achieved by random forecasts" (Wilks 1995). However, these skills scores differ in that the KSS requires unbiased random forecasts. Results arising from these calculations are given in Tables 6 and 7, with the most significant findings discussed below.

4.2.3 Analysis results

For the four days examined in this study, the HCA outperforms the HDA in terms of overall accuracy and skill (cf. Tables 6, 7). This interpretation arises because optimally, conditional probabilities of the same classification and observation type will be near 100% (e.g., POD), whereas conditional probabilities of different classification and observation type will be near zero (e.g., FAR; cf. Tables 6, 7). And, ideally the HSS, KSS, and CSI will be closer to one than zero. The most striking performance improvement for the HCA (relative to the HDA) is a 51% increase in HSS and KSS. These improved scores mean that, compared to the HDA, the HCA classifies the presence and absence of hail significantly better than a random or unbiased random forecast. Another set of notable results are a 46% decrease in the probability of false detection (POFD or $P(Y_1,O_2)$) and a 46% increase in the probability of attaining a correct null, given that hail was forecast ($P(Y_2,O_2)$). Concerning more traditional measures, the HCA shows a 6% increase in POD, a 31% decrease in FAR, and a 30% increase in CSI. In summary, NSSL's HCA provides superior overall performance compared to the HDA. Although these statistics

show that the HCA attains superior overall performance compared to the HDA, algorithm performance varies on individual days. The relative performance of these algorithms for each day is discussed below.

Table 6: HCA accuracy and skill measures, given as percentages, excluding CSI, HSS, and KSS, which range from 0 to 1. Probabilities are rounded to the nearest integer. Misses negatively impact conditional probabilities with light-gray shading, whereas false alarms negatively impact those with dark-gray shading.

Date (2003)	**Hit Rate**	**CSI**	**$P(Y_1,O_1)$**	**$P(Y_1,O_2)$**	**$P(Y_2,O_1)$**	**$P(Y_2,O_2)$**
May 1	100	1	100	0	0	100
May 14	100	1	100	0	0	100
May 19–20	96	0.94	94	0	5	100
June 10–11	73	0.55	83	33	17	67
Total Score	91	0.86	94	12	6	88
Date (2003)	**$P(O_1,Y_1)$**	**$P(O_1,Y_2)$**	**$P(O_2,Y_1)$**	**$P(O_2,Y_2)$**	**HSS**	**KSS**
May 1	100	0	0	100	1	1
May 14	100	0	0	100	1	1
May 19–20	100	10	0	90	0.91	0.94
June 10–11	63	14	37	86	0.47	0.50
Total Score	91	8	8	91	0.82	0.82

Table 7: HDA accuracy and skill measures, given as percentages, excluding CSI, HSS, and KSS, which range from 0 to 1. Probabilities are rounded to the nearest integer. Misses negatively impact conditional probabilities with light-gray shading, whereas false alarms negatively impact those with dark-gray shading.

Date (2003)	**Hit Rate**	**CSI**	**$P(Y_1,O_1)$**	**$P(Y_1,O_2)$**	**$P(Y_2,O_1)$**	**$P(Y_2,O_2)$**
May 1	100	1	100	0	0	100
May 14	75	0.57	57	0	43	100
May 19–20	72	0.71	96	90	4	10
June 10–11	53	0.37	100	71	0	29
Total Score	66	0.56	88	58	12	42
Date (2003)	**$P(O_1,Y_1)$**	**$P(O_1,Y_2)$**	**$P(O_2,Y_1)$**	**$P(O_2,Y_2)$**	**HSS**	**KSS**
May 1	100	0	0	100	1	1
May 14	100	38	0	63	0.53	0.57
May 19–20	74	50	26	50	0.08	0.06
June 10–11	38	0	63	100	0.19	0.28
Total Score	61	22	39	78	0.31	0.31

Measures of forecast accuracy and skill in Tables 6 and 7 show that the performance of the HCA and HDA varies with storm type. Interestingly, both algorithms attain perfect scores on 1 May 2003. On this day, a chase vehicle intercepted an isolated storm as the storm moved eastward from approximately 140 km to 130 km west-northwest of KOUN. During this period (~1hr) the storm dropped pea to marble-size hail at the ground. This result indicates that, given

robust signatures within mid-levels of the storm, and constant phase as these ice particles fall to the ground, both algorithms can successfully detect relatively small size hail using radar data located at distances far from KOUN.

A different situation arises on the morning of 14 May 2003, where the HCA significantly outperforms the HDA by attaining perfect scores. During the morning, a chase vehicle intercepted a storm within a west-to-east-oriented convective line 50–55 km west of KOUN. Although large hail (up to 5") was produced by nearby storm, the intercepted storm produced small hail only (size was missing from the ground truth observations). The performance of the HDA suffers during this event owing to several misses by the algorithm. As a result, the POD, Hit Rate, CSI, and skill scores are relatively low compared to the HCA. Although the HDA has several misses, it produces no false alarms. Thus, like the HCA, the HDA achieves perfect scores in the four accuracy measures influenced by false alarms.

On 19–20 May 2003, chase vehicles intercept a classic supercell, located about 90 km south of KOUN, that drops up to 1.75" hail on the ground. This supercell produces hail cyclically over a several hours, as it moves eastward. Interestingly, the HDA experiences a change in performance, compared to 14 May 2003. In this case, the algorithm endures several false alarms and only one miss. This switch in output yields a high POD (96%), but also a high POFD (90%). The large number of false alarms reduces the HDA's HSS and KSS to near zero. Thus, in this case, the HDA is about as skillful as a random forecast. Since the HCA has only one miss, it outperforms the HDA, mostly in terms of skill (HSS=0.91, KSS=0.94; Table 6). The superior performance of HCA, compared to the HDA, is especially significant in this case, owing to the large hail produced by the storm.

The June 10–11 event is distinguished from previous cases in that chase vehicles intercept storm cells within a line, rather than individual storm cells. In this case, the HCA suffers more misses than false alarms, whereas the HDA suffers from a few false alarms only. As a result, compared to the HCA, the HDA achieves a higher POD and lower probabilities of observing or detecting hail, given that hail is not detected or observed, respectively. On the other hand, compared to the HDA, the HCA achieves lower POFD and FAR, and higher probabilities of attaining a correct null detection or observation, given that hail is not observed or detected by the HCA. Thus, neither algorithm is a clear "winner" in this situation, unless one set of accuracy measures is more detrimental to operations than the other. However, if a user is concerned with skill, the HCA achieves superior scores.

In summary, a comparison of accuracy and skill measures for four cases show that the HCA outperforms the HDA in terms of overall scores and in most storm situations. Nonetheless, situations where the HCA fails to identify hail, even though it is observed, need to be investigated further to advance our understanding of the HCA, and ultimately promote its performance. These positive results, coupled with the HCA's ability to pinpoint the location of hail within a storm, shows that HCA is an advantageous investment for weather-sensitive operations.

4.3 Mesoscale Convective Systems

Over the course of the JPOLE campaign, data were collected for 12 Mesoscale Convective Systems (MCSs). Due to the large size of these systems and the difficulty in obtaining in-situ microphysical information that might be used to verify hydrometeor classification, a comprehensive examination of the utility of the HCA to identify hydrometeor classes in MCSs is beyond the scope of this report. Nevertheless, we do present a case example to demonstrate the ability of the polarimetric radar to identify precipitation regimes within an

MCS, identify the location of the radar bright band, and to discriminate between meteorological and non-meteorological scatterers.

Fig. 13 shows 0.5° base scan data extending to a range of approximately 300 km from an MCS that passed through central Oklahoma on June 16, 2002. In this figure, we present results from application of the "winter" classification algorithm to show the ability of the polarimetric hydrometeor classification to identify the location of the radar bright band (analogous to identification of the rain/snow transition zone in winter precipitation). At this time, the MCS was beginning to enter its dissipative stage, with the convective line still producing heavy rainfall but very little hail. The region of heavy rainfall, as indicated by both large Zs (upper left corner of Fig. 13) and K_{DP}s (not shown), is clearly evident in the HCA output (lower right corner of Fig. 13) in the SW corner of OK (along the convective line).

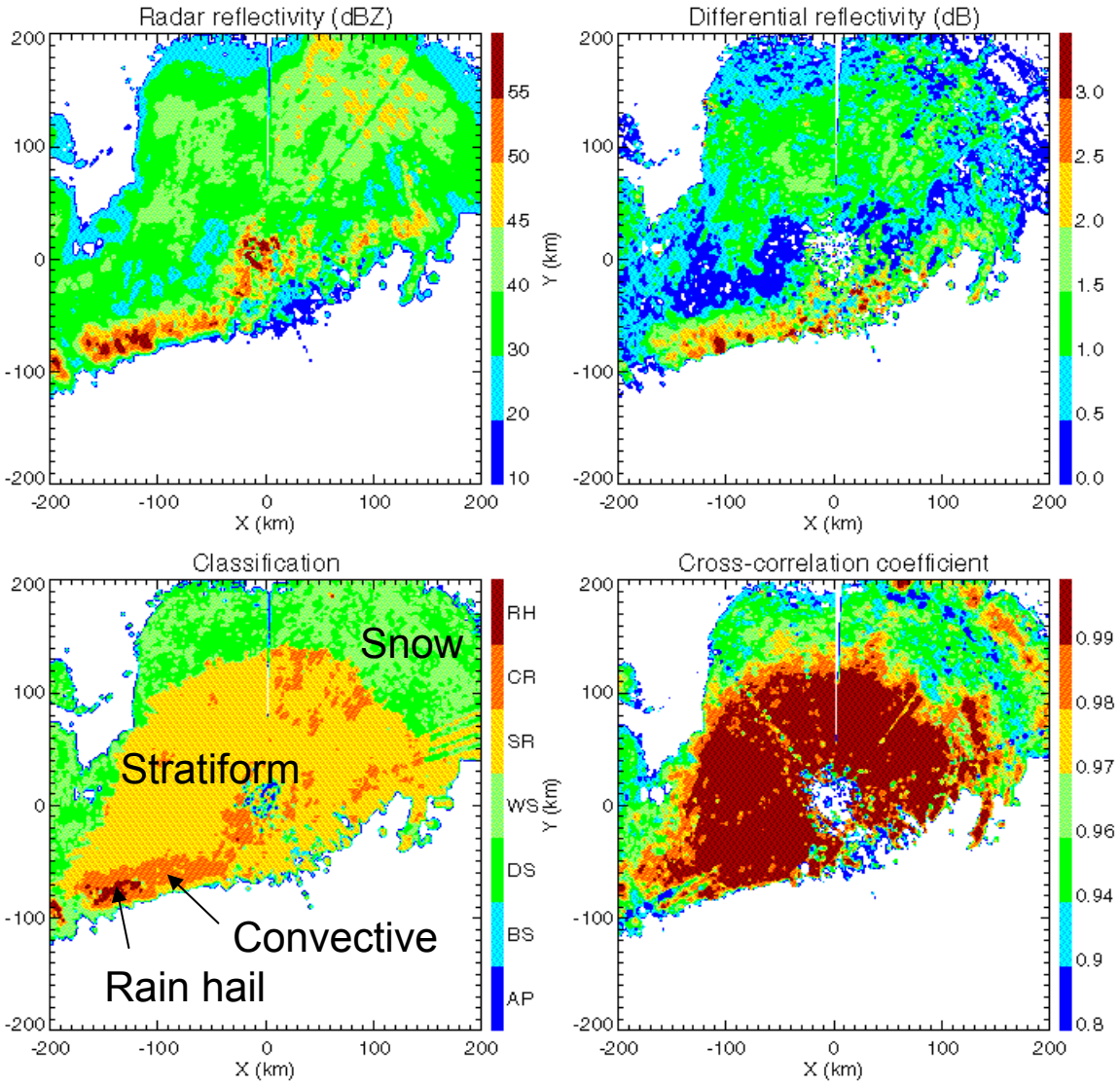

Figure 13: Four panel image of an MCS that passed through central Oklahoma on June 16, 2002: (upper left) reflectivity, (upper right) differential reflectivity (Z_{DR}), (lower left) hydrometeor classification algorithm results, and (lower right) cross-correlation coefficient (ρ_{hv}). Image is at 0232 UTC.

The location of the bottom of the radar bright band is clearly indicated by the somewhat higher Z_{DR}s and dramatic drop in ρ_{hv} (to values that were occasionally < 0.9). Since rainfall in the radar bright band is frequently overestimated by conventional R(Z) rainfall estimation techniques, the ability to identify the location of the radar bright band has many practical applications.

Schuur et al. (2003b) show the results for the same system, but using the "summer" classification algorithm (Section 2.2). The HCA also indicates an extensive region classified as "big drops" along the leading edge of the convective line. This feature is particularly evident in SW Oklahoma, where Z_{DR}s often exceed 4 dB. Regions of big drops are common features at the leading edge of convective cells. Our ground-based observations with a video disdrometer indicate that the high Zs associated with these large, but relatively sparse drops can often lead to overestimation of rain by as much as a factor of ten if a R(Z) relation is used. An extensive region of light to moderate rain is indicated by the HCA in the MCS trailing stratiform region.

4.4 Winter storms

The KOUN radar collected polarimetric data for 4 snow storms during JPOLE: on 3 – 4 December 2002, 6 February 2003, 23 February 2003, and 24 February 2003. These snow events encompass wide variety of different snow types including heavy convective wet snow associated with intense electrical activity (24 February 2003), crystallized snow in very cold air pool (6 February 2003), and more common aggregated dry snow observed on 3 – 4 December 2002 and 23 February 2003. Some results of preliminary polarimetric analysis of the snow storms that occurred on 3 – 4 December 2002 and 24 February 2003 are reported by Ryzhkov and Zrnic (2003), Scharfenberg and Maxwell (2003), and Miller and Scharfenberg (2003).

The performance of the classification algorithm is demonstrated on the winter storm of 3 – 4 December 2002 (Fig. 14). This storm was associated with the passage of a cold front accompanied by the transition from rain to freezing rain and snow in the Oklahoma City metropolitan area. During this event, the melting layer was slowly subsiding with much lower height of the bright band in the cold air pool N – NW from the radar. This feature is manifested by the pronounced asymmetry of the "rain" area with respect to the radar location.

At 12/03/02 1803 UTC (left column of Fig. 14), differential reflectivity gives clear indication of the bright band in the northern sector. More precise determination of the bright band location is possible from the ρ_{hv} data at the elevation of 1.5°. About nine hours later, the height of the melting layer remained almost the same in the southern sector, but decreased noticeably to the north of the radar. Note the bright band signature in the Z field associated with increase of Z_{DR} and drop in ρ_{hv} in that direction.

At 12/04/02 0302 UTC (right column of Fig. 15), rain was recognized NW of the radar up to distances of 50 – 60 km at the lowest elevation scan. At the same time, surface temperature fell below zero and freezing rain was reported on the ground. This freezing rain caused significant damage in the Oklahoma City metropolitan area.

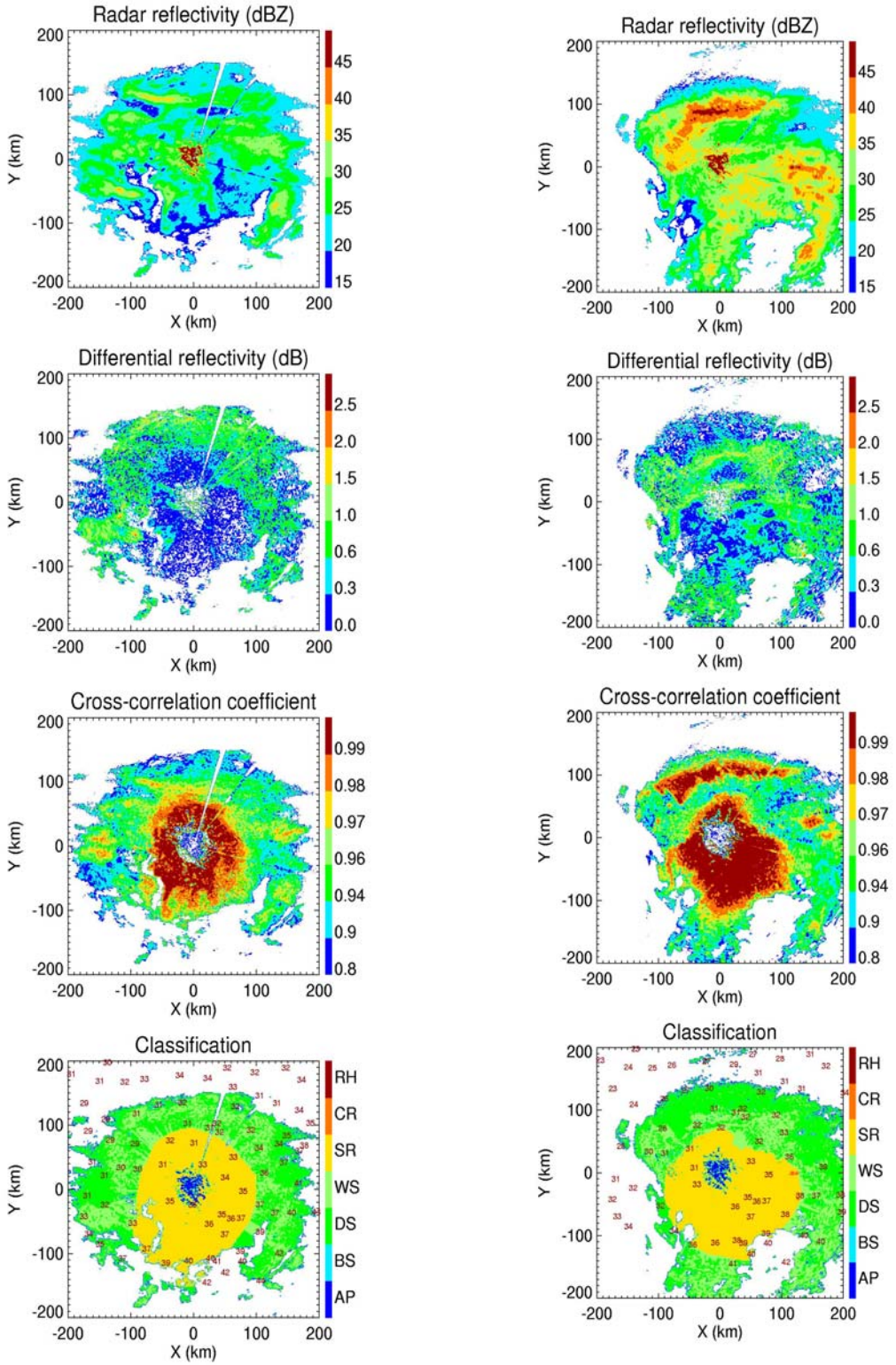

Fig. 14: Composite plots of Z, Z_{DR}, ρ_{hv}, and results of classification at El = 0.5º of the 3 – 4 December snow event at 12/03/02 (left column) and 12/04/02 0302 UTC (right column). Surface temperatures (Fº) are shown in the classification images.

Note that after dropping in the melting layer, the cross-correlation coefficient increases again to attain higher values aloft (where snow is dry) that exceed 0.99. The corresponding lower values of Z_{DR} in dry snow are very similar to those observed in rain below the melting level. This again underlines importance of the bright band identification for separation between dry aggregated snow and light rain.

More detailed meteorological interpretation of polarimetric variables and their use by the forecasters at the Norman NWS office for this winter storm is described by Scharfenberg and Maxwell (2003).

4.5 Non-meteorological scatterers

4.5.1 Polarimetric properties of ground clutter, AP, and biological scatterers

The ability of the polarimetric radar to discriminate between meteorological and non-meteorological scatterers is demonstrated using version 1 of the classification algorithm. As mentioned in section 2.1, this version allows discrimination between three classes of radar scatterers: meteorological, biological, and ground clutter / AP. Five radar variables are used for classification: radar reflectivity Z, differential reflectivity Z_{DR}, cross-correlation coefficient ρ_{hv}, the texture parameter of the radar reflectivity field SD(Z), and the texture parameter of the differential phase field SD(Φ_{DP}). The corresponding membership functions are represented graphically in Fig. 2. These membership functions were obtained after careful analysis of the scatterplots of multiparameter data collected for many hours during several days of observations.

All three classes are heavily overlapped in the Z domain (Fig. 2a). They are much better separated in terms of the other four variables. Differential reflectivity of non-meteorological scatterers varies over wide range. Very high positive Z_{DR} values unambiguously signify biological scatterers (primarily insects), whereas negative Z_{DR}s indicate ground clutter / AP. The separation between the three classes based solely on Z_{DR} is problematic if the measured Z_{DR} is between 0 and 2 dB (Fig. 2b)

The use of cross-correlation coefficient yields very good separation of meteorological and biological scatterers (Fig. 2c). The distinction between weather echoes and ground clutter / AP is not as clear in the ρ_{hv} domain. This can be explained by the fact that non-fluctuating radar signals from man-made objects are characterized by ρ_{hv} very close to 1 (similar to meteorological scatterers), whereas natural land covers (trees, grass, etc.) have very low ρ_{hv}. The cross-correlation of the mixture of man-made and natural scatterers depends on their relative contribution to the radar return in the particular radar resolution volume.

The texture of radar reflectivity (SD(Z)) that is widely used for AP detection with non-polarimetric radars (Kessinger et al. 2001, Steiner and Smith 2002) apparently has value to distinguish meteorological scatterers and ground clutter / AP, but it is not of a great help to isolate the radar echoes from precipitation, insects or birds. The texture of differential phase SD(Φ_{DP}) is more promising than SD(Z) for delineation of precipitation and AP and has less overlap between contributions by meteorological and biological scatterers (Fig. 2d,e).

Although none of the five radar variables provides perfect delineation between three classes, their combination is very efficient if the fuzzy logic approach is used for classification. This complementary character of multiparameter information is illustrated in Fig. 15 where the fields of 6 variables are displayed at the lowest elevation tilt of 0.5º for the case of 13 August

2002 (when all three sources of radar echo produced significant returns). In addition to the five radar variables mentioned, differential phase Φ_{DP} is displayed. Differential phase promises to be a very valuable recognition variable provided that (a) the forward and backward propagation components are separated in Φ_{DP} and (b) the differential phase is measured unambiguously between 0º and 360º (this will be possible on the RVP8 system). We therefore plan to add Φ_{DP} to the classification scheme in the near future.

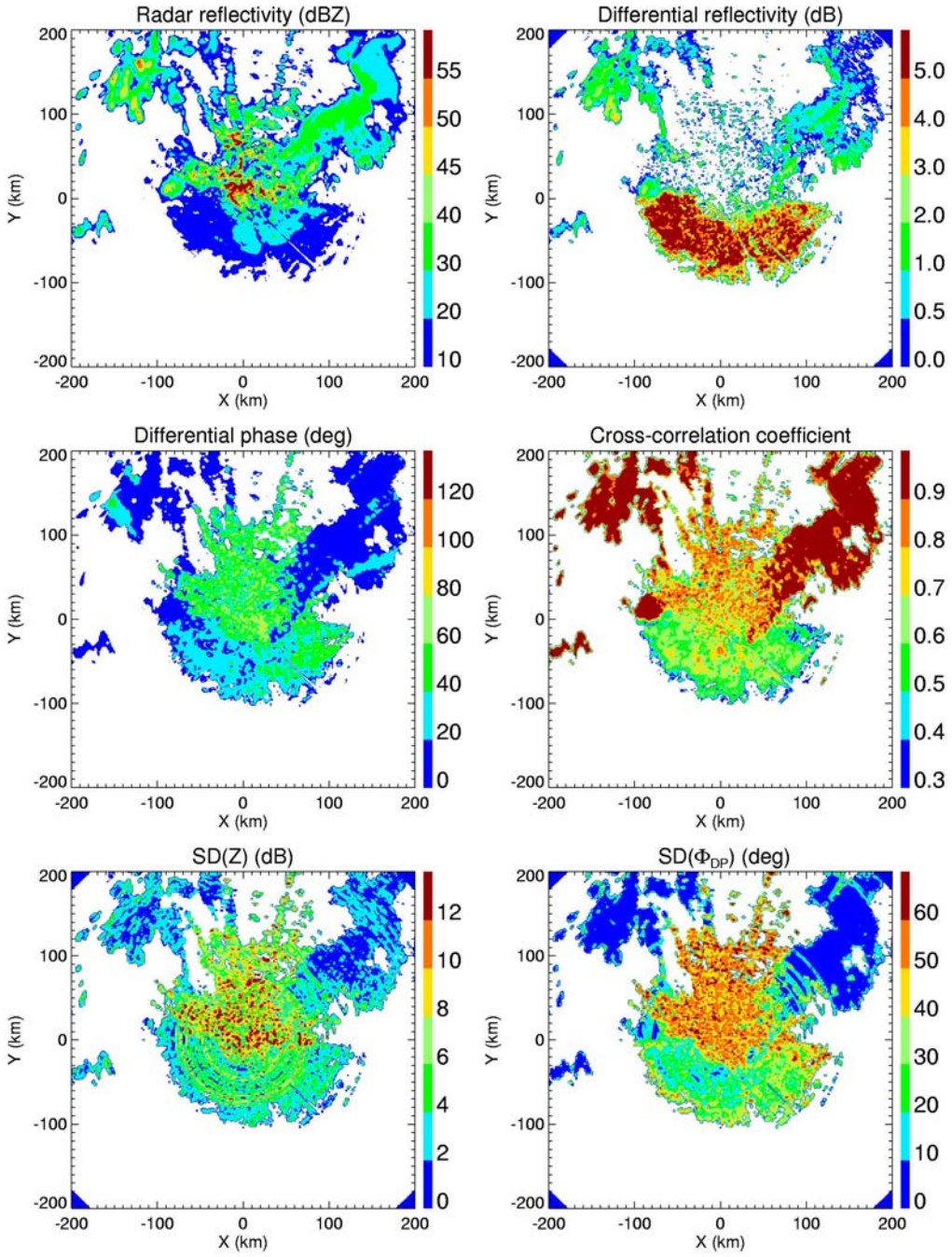

Fig. 15: Composite plot of Z, Z_{DR}, ρ_{hv}, Φ_{DP}, SD(Z), and SD(Φ_{DP}) at El = 0.5º on 13 August 2002, 1024 UTC.

The latter requires some explanation. An intrinsic differential phase of the radar signal due to ground clutter and AP is almost randomly distributed within the interval where the phase is measured (0º – 180º in the RVP7 processor). After radial averaging over 9 successive gates is made, the originally random Φ_{DP} tends to bunch around the middle of the phase interval, i.e., 90º. Unfortunately, the radar signals backscattered from birds have almost the same differential phase (within 70 - 100º). If differential phase is measured in the 0º - 360º interval, then the predominant Φ_{DP} for ground clutter / AP is about 180º and better separation between ground clutter and birds would be achieved.

Examples of classification for the cases of 24 August 2002 and 1 May 2003 are presented in Fig. 16 and 17. In the first case, all three types of radar echoes are mixed together and the radar reflectivity image gives no clue for identification. The classification algorithm identifies extended regions of AP embedded in precipitation. Animation of the classification fields shows high degree of spatial / temporal "coherency" of these fields and gives us more confidence in the performance of the classification scheme. It is interesting to note a difference between regions likely associated with insects (south of the radar) and birds (x = 100, 200 km, y = -150, -30 km) in the SE sector of the image. "Birds" have lower Z_{DR} and higher Φ_{DP} (not shown) than "insects". Also, the "bird" signatures are observed at larger distances and higher altitudes (about 3 km) which are quite unlikely for insect-related echoes. The mean value of Φ_{DP} (due to backscatter differential phase) for "insects" is about 40º, which is substantially lower than the one for "birds".

Fig. 17 illustrates the case with extremely strong AP echo in the SW sector. This echo persisted for about 3 hours and was also observed at the 1.5º elevation angle, although with lesser spatial extension. No rain was recorded by the Oklahoma Mesonet and ARS Micronet gages in this area. Again, the radar reflectivity field gives an impression of strong convective precipitation in the SW sector. Moreover, the presence of AP at higher elevation might confuse traditional AP mitigation schemes, which are based on the Z texture and vertical continuity of the radar echo. The fuzzy logic classification algorithm unambiguously identifies the source of this echo as AP. Less than 1% of radar pixels in this area were wrongly classified as "precipitation" during all three hours of observation of this extreme AP event. At the same time, a thin line of rain in the NE sector was correctly identified as precipitation.

As mentioned in section 3, the quality of classification deteriorates with decreasing signal-to-noise ratio (SNR). In all figures, results of classification are displayed for SNR > 5 dB. Use of differential reflectivity (not biased by noise) in the classification algorithm (together with existing radar variables) might allow us to lower the SNR threshold for reliable classification.

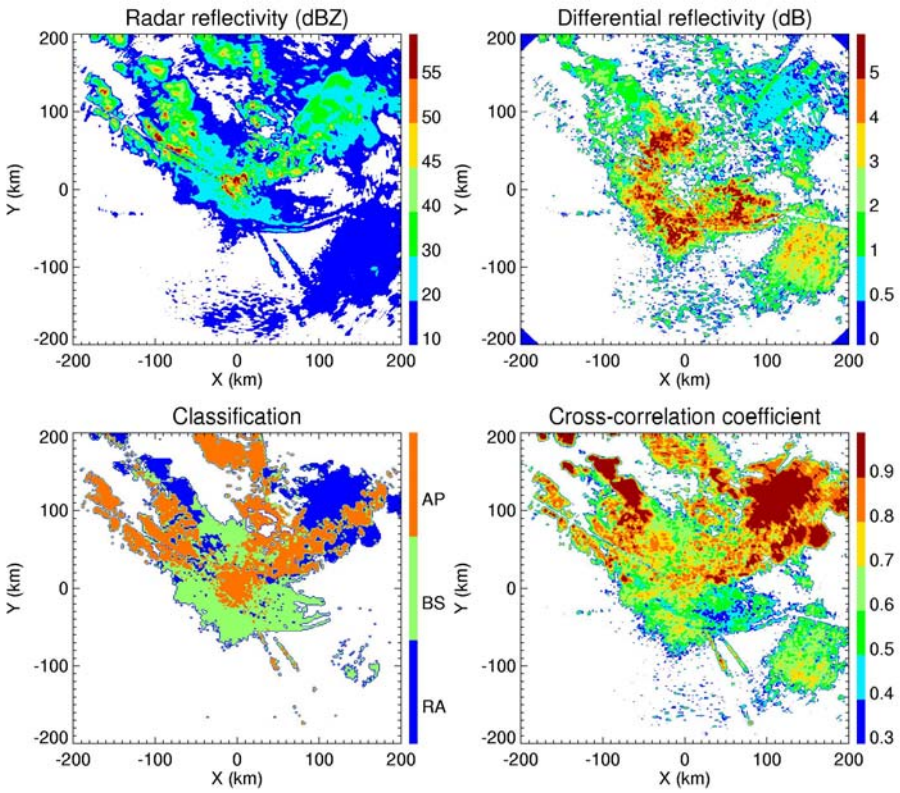

Fig. 16: Composite plot of Z, Z_{DR}, ρ_{hv}, and results of classification at El = 0.5º on 24 August 2002, 0734 UTC.

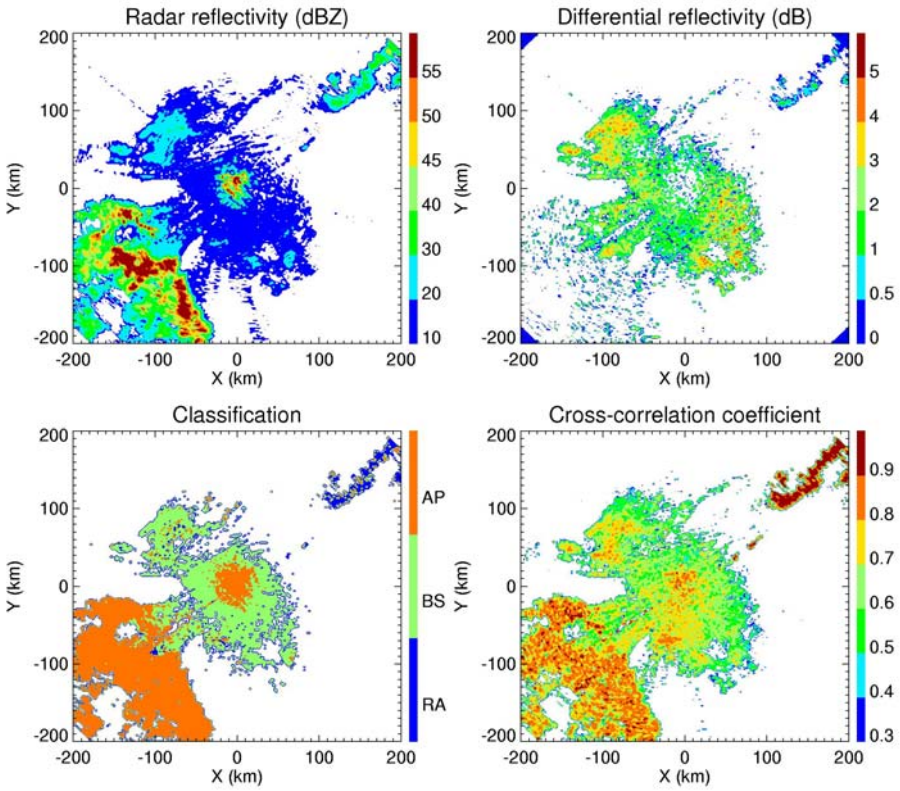

Fig. 17: Composite plot of Z, Z_{DR}, ρ_{hv}, and results of classification at El = 0.5º on 1 May 2003, 1107 UTC.

4.5.2 Polarimetric properties of chaff

In this section, we document an observation of chaff that occurred on Feb 6, 2003. A brief theoretical prediction of differential reflectivity, correlation coefficient, and linear depolarization ratio is given in Zrnic and Ryzhkov (2003). Further theoretical analysis is ongoing, specifically concerning the backscatter differential phase and a comprehensive paper on the subject will be forthcoming.

Chaff is made of aluminum coated thin fibers and is released by the military to create widespread echoes and thus confuse non cooperating tracking radars. To maximize backscattering cross section chaff length is chosen to equal one half the radar wavelength. As predominant wavelengths for military surveillance and tracking are 3, 5, and 10 cm the standard chaff lengths are 1.5, 2.5 and 5 cm. Because chaff is employed by the military as part of routine training in the USA, its echoes are often observed on weather radars (Maddox et al. 1997). Although the reflectivity is relatively weak it is sufficient to contaminate precipitation estimates (Vasiloff and Struthwolf 1997, see the URL at http://www.wrh.noaa.gov/wrhq/97TAs/TA9702/ta97-02.html). Examples abound in Western US whereby chaff is imbedded in precipitation (opus cited) or coexist next to precipitation echoes (Brandt and Atkin 1998, http://www.wrh.noaa.gov/wrhq/98TAs/9804/index.html). Thus it is desirable to recognize returns from chaff and censor these from precipitation products.

It has been argued (Zrnic and Ryzhkov 1999) that polarimetric radar offers a simple and effective way to identify chaff. The argument is rooted in common sense logic and experimental evidence gained with circularly polarized radars (Brooks et al. 1992). Polarimetric signatures of chaff in linear horizontal and vertical basis have not been reported. Moreover, because chaff is a nuisance (as far as observation of weather is concerned), little or no theoretical results about its polarimetric properties are available. Once the polarimetric upgrade of the WSR-88D is achieved it will be possible to have a simple automated procedure for censoring chaff.

In laminar airflow chaff is mostly horizontally oriented and slowly falls with respect to air. Turbulence and differential air motion will cause wobbling. In either case differential reflectivity Z_{DR} is expected to be relatively large. Linear depolarization ratio L_{DR} will increase compared to the value in precipitation and the cross correlation between copolar returns ρ_{hv} will decrease. These polarimetric variables do not depend on the absolute values of returned power (i.e., backscattering cross section), yet they are the most significant discriminators.

Two simple models for computing polarimetric properties of chaff are considered by Zrnic and Ryzhkov (2003). In one the chaff is approximated with the Hertzian dipole so that standard formulas (i.e., for prolate spheroids with induced field along the axis and no field perpendicular) could be applied to compute the elements of the covariance matrix. This approximation is applicable for chaff lengths much shorter than the wavelength. But, for polarimetric variables that are independent of concentration and backscattering cross section, we show that the model can be extended to half wavelength sizes.

The second approach (Zrnic and Ryzhkov 2003) is more realistic because it models chaff as thin cylindrical antenna (to obtain scattering coefficients). Then, once the scattering coefficients are determined, geometrical transformations as done for the spheroids (Bringi and Chandrasekhar 2001, Ryzhkov 2001) are applied for computation of the polarimetric variables.

Chaff is assumed to be uniformly distributed in azimuth. The angle between its axis and horizontal plane (flutter angle) is also uniformly distributed but between zero and a maximum value. The two models produce very similar results if the chaff length is half the radar wavelength or less. The linear depolarization ratio is uniquely related to the ρ_{hv} and Z_{DR} therefore these two variables are sufficient to separate chaff from precipitation echoes. Values of these polarimetric variables as functions of flutter angle are plotted by Zrnic and Ryzhkov (2003).

On 6 February 2003, a cloud of ice crystals (henceforth, snow band) was observed initially over northwest OK, following a snowfall event. This feature advected southeastward toward Oklahoma City (Fig. 19). At the same time, a chaff "cloud" released from an Air Force base in eastern New Mexico moved across southern Oklahoma.

The reflectivity structures of snow band and chaff look very similar but the polarimetric variables exhibit significant differences. Differential reflectivity of chaff ranges from 0 to 6 dB whereas for snow it is 0 to 3 dB, hence there is overlap of values. The fields of correlation coefficient uniquely identify chaff and separate fairly well snow from ground clutter except in regions where SNR in snow is low (at far distances from the radar). Total differential phases of chaff and snow also differ substantially. The differential phase in region of snow is close to the "system" differential phase (of about 30º) and exhibits very small spatial fluctuations. In contrast, differential phase of chaff is characterized by deep spatial variations.

More detailed analysis of the histogram of Φ_{DP}, prior to radial averaging, in chaff reveals broad maximum at about 80º. This mean value of Φ_{DP} might be indicative of a "receiver component" of the "system" differential phase. Indeed, physical considerations show that chaff produces zero backscatter differential phase. That is, regardless of the transmitted differential phase between the H and V components each needle reflects a field aligned along its axis. Thus, upon reflection the H and V fields are in phase. Once these fields are transformed into voltages and subsequently passed through the receiver they acquire the differential phase of the receiver. This reasoning is valid if the H and V fields are transmitted simultaneously, as done in the current implementation on the KOUN radar. In case of sequential transmission (of H and V components) the backscatter differential phase of chaff is equal to the sum of the transmitted differential phase and differential phase of the receiver (i.e., total differential phase of the radar system).

We speculate that very broad distribution of the measured differential phase in chaff is primarily due to high measurement errors attributed to very low cross-correlation coefficient (between 0.2 and 0.5).

Similar analysis of differential phase in ground clutter reveals almost uniform distribution of raw Φ_{DP} within the interval between 0º and 180º. The ρ_{hv} values from ground clutter are significantly higher than the corresponding values from chaff (Fig. 2b), thus one expects smaller measurement errors of Φ_{DP} in ground clutter. The observed uniform distribution of differential phase from ground clutter indicates that its intrinsic Φ_{DP} (i.e., backscatter differential phase void of any measurement errors) might be uniformly distributed as opposed to chaff for which intrinsic differential phase upon scattering is likely zero.

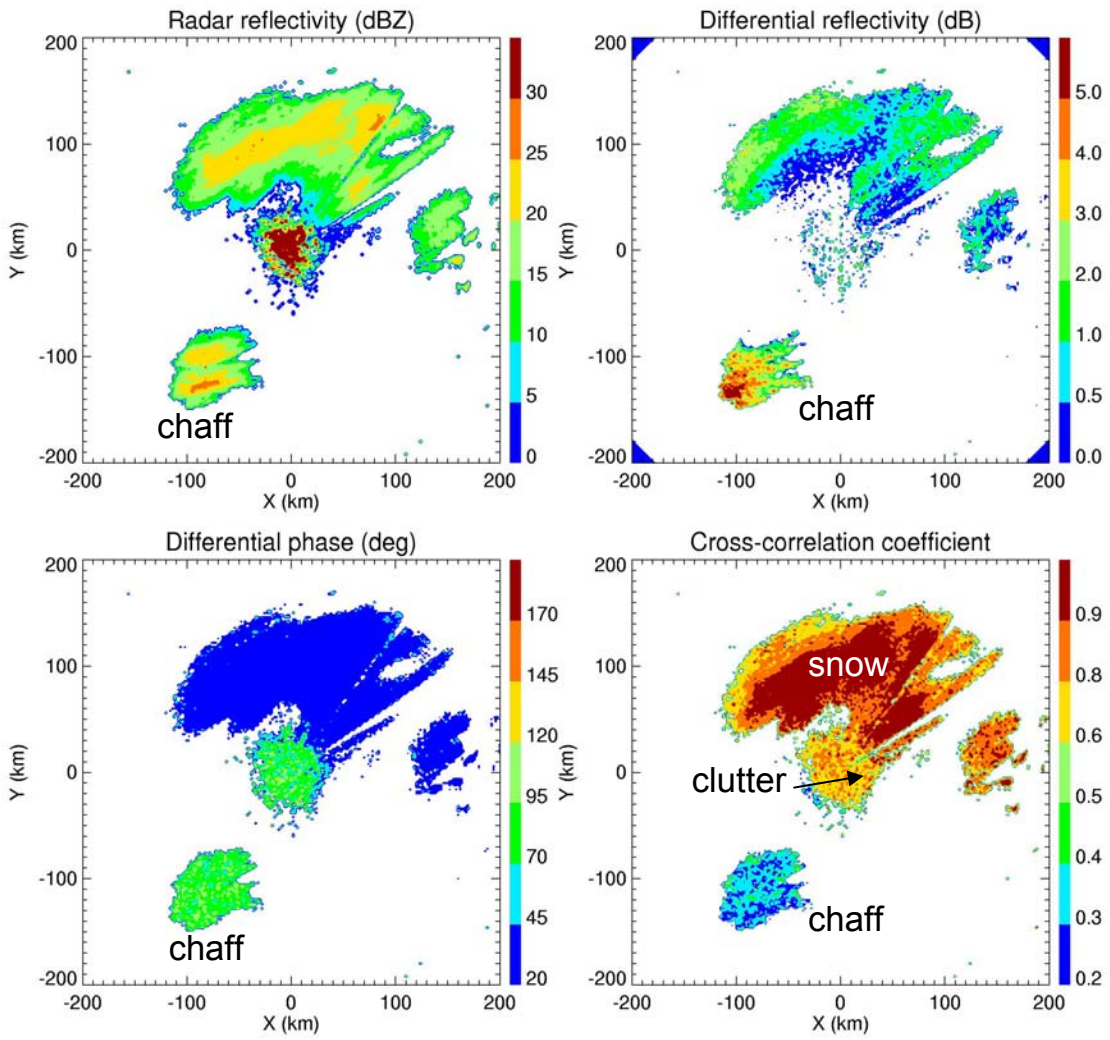

Fig. 18: Fields of polarimetric variables from regions of ground clutter, chaff, and snow. Data were obtained during the JPOLE experiment on Feb 6, 2003. Data is at 2001 UTC and an elevation of 0.5°

Scatterplots of differential reflectivity and correlation coefficient vs. reflectivity factor at SNR > 10 dB and from the region of chaff are displayed in Figs. 20 and 21. These data are from six scans at 0.5° elevation between the times 20 and 21 UTC. The average value of Z_{DR} is 3.36 dB and of ρ_{hv} it is about 0.34. The model with these values (Fig. 1 and Fig. 2 in Zrnic and Ryzhkov 2003) suggests that the flutter angle is 62° (implied from Z_{DR}) and 78° (implied from ρ_{hv}). The agreement is reasonable considering that receiver noise was not accounted for and that the model of uniform flutter angle distribution is a crude approximation of the true (but unknown) distribution. Still both polarimetric variables indicate that the needles have a large effective variation of flutter angles.

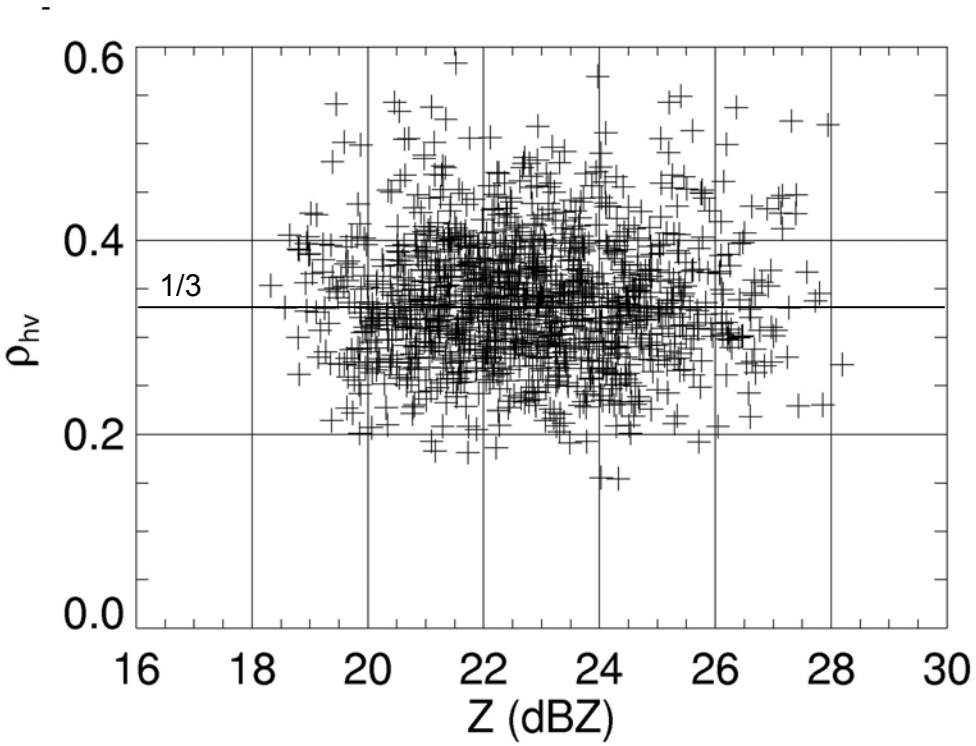

Fig. 19: Scatterplot of the correlation coefficient vs. reflectivity factor from chaff. Data were collected on Feb 6, 2003.

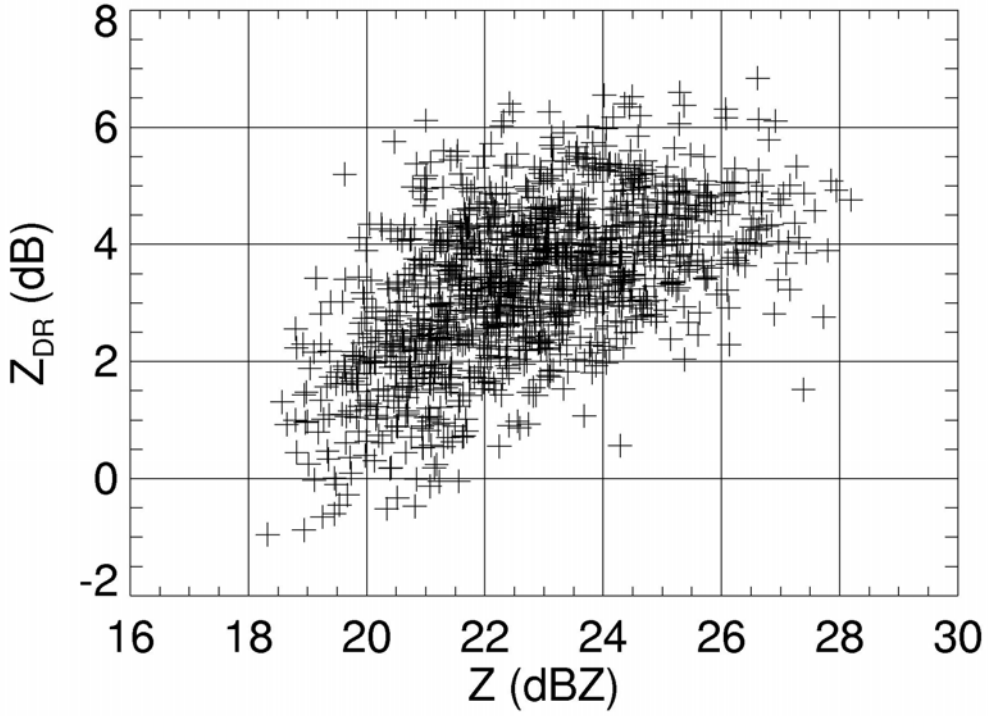

Fig. 20: Scatterplot of differential reflectivity vs. radar reflectivity factor from chaff.

5. Summary

Highly successful data collection during the Joint Polarization Experiment (JPOLE) has provided a large data set that is used to demonstrate the ability of a polarimetric WSR-88D radar to: (1) improve data quality, and (2) improve hydrometeor identification capabilities. Companion reports present an analysis of the calibration and performance of the polarimetric NSSL WSR-88D (Melnikov et al. 2003), an overview of the JPOLE data collection and operational delivery (Schuur et al. 2003a), and an analysis of the ability of a polarimetric WSR-88D to improve rainfall estimation (Ryzhkov et al. 2003).

Three separate fuzzy-logic-based classification algorithms are described and used to conduct the analyses presented in this report. The first algorithm is designed to discriminate between meteorological and non-meteorological scatterers. The second, referred to as the "summer" classification algorithm, identifies hydrometeor types in warm-season precipitation systems. The third, referred to as the "winter" classification algorithm, includes ice categories; it is primarily used to discriminate precipitation type in cold-season precipitation systems (also used to identify the location of the radar bright band in summer precipitation systems).

Three different methods of using polarimetric radar to improve data quality are presented. These include: (1) polarimetric discrimination techniques to filter out non-meteorological echoes, (2) application of Φ_{DP} to increase the accuracy of radar reflectivity measurements or self consistency checks among Z, Z_{DR}, and K_{DP}, and (3) information extraction about biological scatterers to better retrieve Doppler winds in clear air. Conclusions drawn from the application of these methods are summarized below:

- *Filtering out non-meteorological echoes:* Using version 1 of the algorithm, we show that non-meteorological scatterers can be correctly identified and removed from meteorological echoes. The analysis indicates that, if the SNR is > 10 dB, the number of pixels classified as non-meteorological (meteorological) in pure rain (AP/ground clutter) areas is generally < 1%. Misclassification rates deteriorate to approximately 5% if a SNR threshold of > 5 dB is used.

- *Improving the accuracy of reflectivity measurements:* We show that polarimetric data can be used to improve radar reflectivity measurements. With the first technique, differential phase is used to directly correct Z for a case of extreme attenuation along a squall line. With the second technique, a self consistency check that utilizes Z, Z_{DR}, and K_{DP} is used to demonstrate that it is possible to correct Z to within 1.0 to 1.5 dB for cases of poor calibration and/or partial beam blockage (Ryzhkov et al. 2003).

- *Improving Doppler wind measurements in clear air:* Most clear echoes are caused by biological scatterers such as birds and insects. Polarimetric radar can discriminate between the two and thus identify contaminated Doppler wind estimates.

Examples of classification techniques to identify regions of AP/ground clutter, biological scatterers, and chaff are also presented in this report.

The analyses also demonstrate the ability of polarimetric classification techniques to improve hydrometeor discrimination (as well as identify the location of non-meteorological scatterers that are embedded within meteorological echoes). Examples are provided for 4 different types of precipitation systems. These include the ability to: (1) detect tornadic debris,

(2) identify the location of hail, (3) identify hydrometeor types (and the location of the radar bright band) in an MCS, and (4) identify hydrometeor types (and the location of the rain/snow line) for a winter storm. These applications are summarized below:

- *Detect tornado debris:* An investigation of two significant tornado events that occurred close to the KOUN radar during JPOLE provide confirmation of repeatable polarimetric signatures associate with tornadic debris. Several conclusions can be drawn from this work. For example, polarimetric data can confirm tornado warnings, confirm tornado damage, and pinpoint current tornado location. Additional data collection and research is required to determine whether polarimetric radar data can be used to detect tornadic debris at distant ranges or to identify polarimetric signatures that might be associated with possible microphysical precursors to tornadogenesis.

- *Identify the location of hail:* The presented data to demonstrate the ability of polarimetric radar to improve hail detection. Previous radar-based hail algorithms only provide estimates of hail (or severe hail) probability for any given storm. On the other hand, the polarimetric classification algorithm pinpoints hail location within the storm. A statistical analysis presented in this report demonstrates the advantages provided by the polarimetric classification algorithm. The analysis results indicate that the polarimetric Hydrometeor Classification Algorithm (HCA) outperforms the operational Hail Detection Algorithm (HDA) in terms of both overall accuracy and skill (Section 4.2.3). Whereas the statistics show that the HCA attains superior overall performance compared to the HDA, the algorithm performance varies on individual days. Additional research is required to enhance algorithm performance, identify microphysical signatures that might be associated with hail embryo regions, and to determine hail size.

- *Identify hydrometeor type in an MCS:* Application of the hydrometeor classification algorithm to a MCS demonstrates the ability of the polarimetric hydrometeor classification algorithm to identify hydrometeor types in a large, warm-season precipitation system. The algorithm also shows great utility for locating the bright band, which is a region where rainfall is often greatly overestimated by conventional R(Z) relations. Additional research is required to gather information that might boost algorithm performance, as well as provide data that could justify inclusion of additional ice categories in the classification scheme.

- *Identify hydrometeor type in a winter storm:* Application of the hydrometeor classification algorithm to a winter storm demonstrates the ability of the polarimetric hydrometeor classification algorithm to identify hydrometeor types in a large, cold-season precipitation system. The algorithm also shows great utility at determining the location of the rain/snow transition line.

During JPOLE, several polarimetric KOUN WSR-88D radar measurements and hydrometeor classification products were delivered to operational forecasters at the Norman, OK NWS forecast office. Application of these data and products in the warning decision process is discussed by Schuur et al. (2003a).

References

Brandt M. B., and D. V. Atkin, 1998: Chaff in the vicinity of thunderstorms in Southern California on 6 June 1997. NWS, Western Region Technical Attachment No. 98-04 February 3, 1998.

Bringi, V. N., V. Chandrasekar, N. Balakrishnan, and D. Zrnic, 1990: An examination of propagation effects on radar measurements at microwave frequencies. J. Atmos. Oceanic Technol., 7, 829 – 840.

Bringi, V. N. and V. Chandrasekar, 2001: Polarimetric Doppler Weather Radar, Principles and Applications. Cambridge University Press, Cambridge, UK, p. 636.

Brooks, E. M., J. D. Marwitz, and R. A. Kropfli, 1992: Radar Observations of transport and diffusion in clouds and precipitation using TRACIR. *J. Atmos. Oceanic. Technol.* **9,** 226-241.

Goddard, J., J. Tan, and M. Thurai, 1994: Technique for calibration of meteorological radars using differential phase. *Electronic Letters*, **30**, 166 – 167.

Gorgucci, E., G. Scarchilli, and V. Chandrasekar, 1999: A procedure to calibrate multiparameter weather radar using properties of the rain medium, *IEEE Trans. Geosci. Remote Sensing*, **37**, 269 – 276.

Gourley, J., B. Kaney, and R. Maddox, 2003: Evaluating the calibrations of radars: a software approach. Preprints*, 31st International Conference on Radar Meteorology,* Seattle, 459 – 462.

Johnson, J. T., MacKeen, P. L., Witt, A., Mitchell, E. D., Stumpf, G. J., Eilts, M. D., Thomas, K. W. 1998: The Storm Cell Identification and Tracking Algorithm: An Enhanced WSR-88D Algorithm. *Wea. Forecasting,* **13**, 263–276.

Kessinger, C., S. Ellis, and J. Van Andel, 2001: NEXRAD data quality: the AP clutter mitigation scheme. Preprints, *30th International Conference on Radar Meteorology,* Munich, Germany, 707 – 709

Liu, H. and V. Chandrasekar, 2000: Classification of hydrometeors based on polarimetric radar measurements: development of a fuzzy logic and neuro-fuzzy systems, and in situ verification, *J. Atmos. Oceanic Technol*., **17**, 140-164.

Maddox, R.A., Kenneth W. Howard, and Charles L. Dempsey, 1997: Intense Convective Storms with Little or No Lightning over Central Arizona: A Case of Inadvertent Weather, Modification? *J. Appl. Meteor.,* **36,** 302-314.

Melnikov, V., D. Zrnic, , R. Doviak, and J. Carter, 2003: Calibration and performance analysis of NSSL's polarimetric WSR-88D. Report of the National Severe Storms Laboratory, Norman, OK, 73069, 77 pp.

Miller, D. and K. Scharfenberg, 2003: The use of polarimetric radar data in the winter weather warning decision making process: a case study. Preprints*, 31st International Conference on Radar Meteorology,* Seattle, 976 – 979.

Moszkowicz, S., G. Ciach, and W. Krajewski, 1994: Statistical detection of anomalous propagation in radar reflectivity patterns. *J. Atmos. Oceanic Technol*., **11**, 1026 – 1034.

Ryzhkov, A., and D. Zrnic, 1995: Precipitation and attenuation measurements at a 10 cm wavelength. *Journal of Applied Meteorology,* **34**, 2121-2134.

Ryzhkov, A., and D. Zrnic, 1998: Discrimination between rain and snow with a polarimetric radar, *J. Appl. Meteor*., **37**, 1228-1240.

Ryzhkov, A.V., 2001: Interpretation of polarimetric radar covariance matrix for meteorological scatterers: Theoretical analysis. *J. Atmos. Oceanic. Technol.* **18,** 315-328.

Ryzhkov, A.., S. Giangrande, D. Zrnic, 2002a: Using multiparameter data to calibrate polarimetric weather radars in the presence of a partial beam blockage. Proc. IGARSS 2002, Toronto, Canada, 2820 – 2822.

Ryzhkov, A.V., D. Burgess, D. Zrnic, T. Smith, and S. Giangrande, 2002b: Polarimetric analysis of a 3 May 1999 tornado. *Preprints, 21st Conference on Severe Local Storms*, San Antonio, 515-518.

Ryzhkov, A. and D. Zrnic, 2003: Discrimination between rain and snow with a polarimetric NEXRAD radar. Preprints, *31st International Conference on Radar Meteorology,* Seattle, 635 - 638.

Ryzhkov, A., S. Giangrande, and T. Schuur, 2003: *Rainfall measurements with the polarimetric WSR-88D radar.* Report of the National Severe Storms Laboratory, Norman, OK, 73069, 98 pp.

Scharfenberg, K., and E. Maxwell, 2003: Operational use of a hydrometeor classification algorithm to detect the snow melting level. Preprints, *31st International Conference on Radar Meteorology,* Seattle, 639 – 641.

Schuur, T., P. Heinselman, K. Scharfenberg, A. Ryzhkov, D. Zrnic, V. Melnikov, and J. Krause, 2003a: Overview of the Joint Polarization Experiment (JPOLE), Report of the National Severe Storms Laboratory, Norman, OK, 73069, 39 pp.

Schuur, T. J., D. S. Zrnic, and R. E. Saffle, 2003b: The Joint Polarization Experiment - An Overview of Initial Data Collection with a Polarimetric WSR-88D Radar. *Preprints, 19th International Conference on Interactive Information and Processing Systems (IIPS),* Long Beach, California, American Meteorological Society, Boston, published on conference CD.

Steiner, M., and J. Smith, 2002: Use of the three-dimensional reflectivity structure for automated detection and removal of nonprecipitating echoes in radar data. *J. Atmos. Oceanic Technol*., **19,** 673 – 686.

Straka, J., D. Zrnic, and A. Ryzhkov, 2000: Bulk hydrometeor classification and quantification using multiparameter radar data. Synthesis of relations. *Journal of Applied Meteorology,* **39**, 1341 - 1372.

Vivekanandan, J., D. Zrnic, S. Ellis, D.Oye, A. Ryzhkov, J. Straka, 1999: Cloud microphysics retrieval using S-band dual-polarization radar measurements. *Bulletin of the American Meteorological Society,* **80**, 381-388.

Vasiloff, S, and M. Struthwolf, 1997: Chaff mixed with radar weather echoes, NWS, Western region technical attachment No. 97-02, January 17, 1997.

Wilks, D. S., 1995: *Statistical Methods in Atmospheric Sciences*. Academic Press. 467 pp.

Witt, A., M. D. Eilts, G. J. Stumpf, J. T. Johnson, E. D. Mitchell, and K. W. Thomas, 1998a (June): An enhanced hail detection algorithm for the WSR-88D. *Wea. Forecasting*, **13**, 286-303.

Zrnic, D., and A. Ryzhkov, 1998: Observations of insects and birds with a polarimetric radar. IEEE Transactions on Geoscience and Remote Sensing, **36**, 661-668.

Zrnic, D., and A. Ryzhkov, 1999 Polarimetry for weather surveillance radars. *Bulletin of the American Meteorological Society,* **80**, 389 - 406.

Zrnic, D. S., and A. Ryzhkov, 1999: Polarimetry for weather surveillance radar. Bulletin of the American Meteorological Society, **80**, 389-406.

Zrnic, D.S., A.V. Ryzhkov, J. Straka, Y. Liu, and J. Vivekanandan, 2001: Testing a procedure for automatic classification hydrometeor types. *Journal of Atmospheric and Oceanic Technology,* **18**, 892 - 913.

Zrnic, D. S., and A. V. Ryzhkov, 2003: Polarimetric properties of chaff. *Preprints, 31st Conference on Radar Meteorology*. Amer. Meteor. Soc., Seattle, WA, 629-631.

Appendix A

We begin with a brief review of the 2x2 contingency table, where *a* is a "hit", *b* is a "false alarm", *c* is a "miss", and *d* is a "correct null" (Table 5). Eight conditional probabilities are available from the classic 2x2 contingency table, defined by $P(F_{i=1,2},O_{i=1,2})$ and $P(O_{i=1,2},F_{i=1,2})$, where P is the conditional probability, F is the algorithm detection, O is ground truth, and the subscript i denotes either the presence (i=1) or absence (i=2) of a given phenomena (here hail) in the algorithm detection and ground truth. The equations denoting these probabilities and a brief description of each are given below. These descriptions apply to the hail verification within this report.

The first set of conditional probabilities relate the probability of attaining a "yes" or "no" detection, given the observation:

1. $P(Y_1, O_1) = \frac{a}{a+c}$ is the probability of attaining a hit, given that hail was observed. This conditional probability is known as the probability of detection (POD).

2. $P(Y_1, O_2) = \frac{b}{b+d}$ is the probability of attaining a false alarm, given that hail was not observed. This measure is known as the probability of false detection (POFD).

3. $P(Y_2, O_1) = \frac{c}{a+c}$ is the probability of attaining a miss, given that hail is observed.

4. $P(Y_2, O_2) = \frac{d}{b+d}$ is the probability of attaining a correct null, given that hail was not observed.

This second set of conditional probabilities relate the probability of observing hail or a lack thereof, given the detection:

1. $P(O_1, Y_1) = \frac{a}{a+b}$ is the probability of hail being observed, given that the algorithm detected hail.

2. $P(O_1, Y_2) = \frac{c}{c+d}$ is the probability of hail being observed, given that the algorithm did not detect hail.

3. $P(O_2, Y_1) = \frac{b}{a+b}$ is the probability of no hail being observed, given that the algorithm detected hail. This measure is known as the false alarm rate (FAR).

4. $P(O_2, Y_2) = \frac{d}{b+d}$ is the probability of no hail being observed, given that the algorithm did not detect hail.